

Testing non-standard neutrino matter interactions in atmospheric neutrino propagation

Animesh Chatterjee^{* a}, Poonam Mehta^{† b}, Debajyoti Choudhury^{◇ c} and Raj Gandhi^{‡ d}

^{*} *Department of Physics, University of Texas at Arlington, Arlington, TX 76019, USA*

[†] *School of Physical Sciences, Jawaharlal Nehru University, New Delhi 110067, India*

[◇] *Department of Physics and Astrophysics, University of Delhi, Delhi 110007, India*

[‡] *Harish-Chandra Research Institute, Chhatnag Road, Jhansi, Allahabad 211 019, India*

June 21, 2016

Abstract

We study the effects of non-standard interactions on the oscillation pattern of atmospheric neutrinos. We use neutrino oscillograms as our main tool to infer the role of non-standard interactions (NSI) parameters at the probability level in the energy range, $E \in [1, 20]$ GeV and zenith angle range, $\cos \theta \in [-1, 0]$. We compute the event rates for atmospheric neutrino events in presence of NSI parameters in the energy range $E \in [1, 10]$ GeV for two different detector configurations - a magnetized iron calorimeter and an unmagnetized liquid Argon time projection chamber which have different sensitivities to NSI parameters due to their complementary characteristics.

^aEmail: animesh.chatterjee@uta.edu

^bEmail: pm@jnu.ac.in

^cEmail: debchou@physics.du.ac.in

^dEmail: raj@hri.res.in

1 Introduction

With the immense progress over the past few decades in establishing neutrino masses and mixings, it is fair to say that neutrino physics has entered an era of precision measurements. The first confirmation came in 1998 courtesy the pioneering experiment, Super Kamiokande (SK) [1]. With more data as well as with the aid of numerous other experiments, we have steadily garnered more and more precise information about the neutrino mixing parameters. As a result, the long list of unanswered questions in the standard scenario has become shorter (for recent global analyses of all neutrino oscillation data, see [2–4]). The focus of the ongoing and future neutrino experiments is on resolving the issue of neutrino mass hierarchy *i.e.*, sign $(\delta m_{31}^2)^1$, measuring the CP phase (δ) and determining the correct octant of the mixing angle θ_{23} .

The minimal theoretical scenario needed to describe oscillations requires the existence of neutrino masses. The simplest way is to add right handed neutrino fields to the Standard Model (SM) particle content (something that the originators of the SM would, no doubt, have trivially done were nonzero neutrino masses known then) and generate a Dirac mass term for neutrinos. However it is hard to explain the smallness of the neutrino mass terms via this mechanism. To overcome this, an attractive way is to add dimension-five non-renormalizable terms consistent with the symmetries and particle content of the SM, which naturally leads to desired tiny Majorana masses for the left-handed neutrinos². However in the minimal scenario of this extension, the dominant neutrino interactions involving the light fields are still assumed to be described by weak interactions within the SM in which flavour changes are strongly suppressed.

Once we invoke new physics in order to explain the non-zero neutrino masses, it seems rather unnatural to exclude the possibility of non standard interactions (NSI) which can, in principle, allow for flavour changing interactions. Simultaneously, these are new sources of CP violation which can affect production, detection and propagation of neutrinos [5]. Some of the early attempts discussing new sources of lepton flavour violation (for instance, R -parity violating supersymmetry) were geared towards providing an alternate explanation for the observed deficit of neutrinos in the limiting case of zero neutrino masses and the absence of vacuum mixing [6,7]. In recent years, the emphasis has shifted towards understanding the interplay between the standard electroweak interactions (SI) and NSI and whether future oscillation experiments can test such NSI apart from determining the standard oscillation parameters precisely. This has led to an upsurge in research activity in this area (see the references in [5]). This is also interesting from the point of view of complementarity with the collider searches for new physics. There are other motivations for NSI as well such as (electroweak) leptogenesis [8], neutrino magnetic moments [9–12], neutrino condensate as dark energy [13,14].

Neutrino oscillation experiments can probe NSI by exploiting the interference with the Stan-

¹ $\delta m_{31}^2 = m_3^2 - m_1^2$.

²Terms such as $\bar{\nu}_{Ri}^c \nu_{Rj}$ are gauge invariant too and phenomenologically unconstrained. While they break lepton number, the latter is only an accidental symmetry in the SM. Thus, such terms, in conjunction with the usual Dirac mass terms, would generate tiny observable neutrino masses through the see-saw mechanism. It can be readily seen that, the aforementioned dimension-five term $(\bar{L}^c L \phi \phi)$ essentially mimics this mechanism in the low energy effective theory.

standard Model amplitude. In view of the excellent agreement of data with standard flavour conversion via oscillations, we would like to explore the extent to which NSI (incorporated into the Lagrangian phenomenologically via small parameters) is empirically viable, with specific focus on atmospheric neutrino signals in future detectors. NSI in the context of atmospheric neutrinos has been studied by various authors [15–19]. Also there are studies pertaining to other new physics scenarios using atmospheric neutrinos such as CPT violation [20, 21], violation of the equivalence principle [22], large extra dimension models [23] and sterile neutrinos [24–26].

The plan of the article is as follows. We first briefly outline the NSI framework in Sec. 2 and subsequently discuss the neutrino oscillation probabilities in presence of NSI using the perturbation theory approach (in Sec. 3). We describe the features of the neutrino oscillograms in Sec. 4. We give the details of our analysis in Sec. 5 and the discussion on events generated for the two detector types in Sec. 6. Finally, we conclude in Sec. 7.

2 Neutrino NSI Framework: relevant parameters and present constraints

As in the case of standard weak interactions, a wide class of “new physics scenarios” can be conveniently parameterised in a model independent way at low energies ($E \ll M_{EW}$, where M_{EW} is the electroweak scale) by using effective four-fermion interactions. In general, NSI can impact the neutrino oscillation signals via two kinds of interactions : (a) charged current (CC) interactions (b) neutral current (NC) interactions. However, CC interactions affect processes only at the source or the detector and these are clearly discernible at near detectors (see for example, [27, 28]). On the other hand, the NC interactions affect the propagation of neutrinos which can be studied only at far detectors. Due to this decoupling, the two can be treated in isolation. Usually, it is assumed that the CC NSI terms (*e.g.*, of the type $(\bar{\nu}_\beta \gamma^\mu P_L l_\alpha)(\bar{f}_L \gamma_\mu P_C f'_L)$ with f, f' being the components of a weak doublet) are more tightly constrained than the NC terms and, hence, are not considered. It turns out, though, that, in specific models, the two can be of comparable strengths [29]. However, since we are interested in NSI that alter the propagation of neutrinos, we shall consider the NC type of interactions alone.

The effective Lagrangian describing the NC type neutrino NSI of the type $(V - A)(V \pm A)$ is given by³

$$\mathcal{L}_{NSI} = -2\sqrt{2}G_F \varepsilon_{\alpha\beta}^{fC} [\bar{\nu}_\alpha \gamma^\mu P_L \nu_\beta] [\bar{f} \gamma_\mu P_C f] , \quad (1)$$

where G_F is the Fermi constant, ν_α, ν_β are neutrinos of different flavours, and f is a first generation SM fermion (e, u, d)⁴. The chiral projection operators are given by $P_L = (1 - \gamma_5)/2$ and $P_C = (1 \pm \gamma_5)/2$. If the NSI arises at scale $M_{NP} \gg M_{EW}$ from some higher dimensional operators (of order six or higher), it would imply a suppression of at least $\varepsilon_{\alpha\beta}^{fC} \simeq (M_{EW}/M_{NP})^2$ (for $M_{NP} \sim 1 \text{ TeV}$, we have $\varepsilon_{\alpha\beta}^{fC} \simeq 10^{-2}$). However, such a naive dimensional analysis argument breaks down if the new physics sector is strongly interacting

³One could think that other Dirac structures generated by intermediate scalar (S), pseudoscalar (P) or tensor (T) fields may also be there. However, these would only give rise to subdominant effects.

⁴Coherence requires that the flavour of the background fermion (f) is preserved in the interaction. Second or third generation fermions do not affect oscillation experiments since matter does not contain them.

as can happen in a variety of models. We shall, hence, admit even larger $\varepsilon_{\alpha\beta}^{fC}$ as long as these are consistent with all current observations. In general, NSI terms can be complex. Naively, $SU(2)$ invariance would dictate that operators involving ν_{Li} must be accompanied by ones containing the corresponding charged lepton field, thereby leading to additional CC interactions. This, however, can be avoided by applying to $SU(2)$ breaking and/or invoking multiple fields and interactions in the heavy (or hidden) sector. Rather than speculate about the origin of any such mechanism, we assume here (as in much of the literature) that no such CC terms exist.

The new NC interaction terms can affect the neutrino oscillation physics either by causing the flavour of neutrino to change ($\nu_\alpha + f \rightarrow \nu_\beta + f$) *i.e.*, flavour changing (FC) interaction or, by having a non-universal scattering amplitude of NC for different neutrino flavours *i.e.*, flavour preserving (FP) interaction. At the level of the underlying Lagrangian, NSI coupling of the neutrino can be to e, u, d . However, from a phenomenological point of view, only the sum (incoherent) of all these individual contributions (from different scatterers) contributes to the coherent forward scattering of neutrinos on matter. If we normalize⁵ to n_e , the effective NSI parameter for neutral Earth matter⁶ is

$$\varepsilon_{\alpha\beta} = \sum_{f=e,u,d} \frac{n_f}{n_e} \varepsilon_{\alpha\beta}^f = \varepsilon_{\alpha\beta}^e + 2\varepsilon_{\alpha\beta}^u + \varepsilon_{\alpha\beta}^d + \frac{n_n}{n_e} (2\varepsilon_{\alpha\beta}^d + \varepsilon_{\alpha\beta}^u) = \varepsilon_{\alpha\beta}^e + 3\varepsilon_{\alpha\beta}^u + 3\varepsilon_{\alpha\beta}^d, \quad (2)$$

where n_f is the density of fermion f in medium crossed by the neutrino and n refers to neutrons. Also, $\varepsilon_{\alpha\beta}^f = \varepsilon_{\alpha\beta}^{fL} + \varepsilon_{\alpha\beta}^{fR}$ which encodes the fact that NC type NSI matter effects are sensitive to the vector sum of NSI couplings.

Let us, now, discuss the constraints on the NC type NSI parameters. As mentioned above, the combination that enters oscillation physics is given by Eq. (2). The individual NSI terms such as $\varepsilon_{\alpha\beta}^{fL}$ or $\varepsilon_{\alpha\beta}^{fR}$ are constrained in any experiment (keeping only one of them non-zero at a time) and moreover the coupling is either to e, u, d individually [30]. In view of this, it is not so straightforward to interpret those bounds in terms of an effective $\varepsilon_{\alpha\beta}$. There are two ways : (a) One could take a conservative approach and use the most stringent constraint in the individual NSI terms (say, use $|\varepsilon_{\mu\tau}^u|$) to constrain the effective term (say, $|\varepsilon_{\mu\tau}|$) in Eq. (2) and that leads to

$$|\varepsilon_{\alpha\beta}| < \begin{pmatrix} 0.06 & 0.05 & 0.27 \\ 0.05 & 0.003 & 0.05 \\ 0.27 & 0.05 & 0.16 \end{pmatrix}. \quad (3)$$

The constraints involving muon neutrinos are at least an order of magnitude stronger (courtesy the NuTeV and CHARM scattering experiments) than those involving electron and tau neutrino [31]. (b) With the assumption that the errors on individual NSI terms are uncorrelated, the authors in Ref. [29] deduce model-independent bounds on effective NC NSI terms

$$\varepsilon_{\alpha\beta} \lesssim \left\{ \sum_{C=L,R} [(\varepsilon_{\alpha\beta}^{eC})^2 + (3\varepsilon_{\alpha\beta}^{uC})^2 + (3\varepsilon_{\alpha\beta}^{dC})^2] \right\}^{1/2}, \quad (4)$$

⁵If we normalize to either up or down quark abundance (assume isoscalar composition of matter) instead, there is a relative factor of 3 which will need to be incorporated accordingly.

⁶For neutral Earth matter, there are 2 nucleons (one proton and one neutron) per electron. For neutral solar matter, there is one proton for one electron, and $\varepsilon_{\alpha\beta} = \varepsilon_{\alpha\beta}^e + 2\varepsilon_{\alpha\beta}^u + 2\varepsilon_{\alpha\beta}^d$

which, for neutral Earth matter, leads to

$$|\varepsilon_{\alpha\beta}| < \begin{pmatrix} 4.2 & 0.33 & 3.0 \\ 0.33 & 0.068 & 0.33 \\ 3.0 & 0.33 & 21 \end{pmatrix}. \quad (5)$$

Note that the values mentioned in Eq. (5) are larger by one or two orders of magnitude than the overly restrictive bounds of Eq. (3), which, of course, need not be applicable.

Apart from the model independent theoretical bounds, two experiments have used the neutrino data to constrain NSI parameters which are more restrictive. The SK NSI search in atmospheric neutrinos crossing the Earth found no evidence in favour of NSI and the study led to upper bounds on NSI parameters [32] given by $|\varepsilon_{\mu\tau}| < 0.033$, $|\varepsilon_{\tau\tau} - \varepsilon_{\mu\mu}| < 0.147$ (at 90% CL) in a two flavour hybrid model [5]⁷. The off-diagonal NSI parameter $\varepsilon_{\mu\tau}$ is constrained $-0.20 < \varepsilon_{\mu\tau} < 0.07$ (at 90% CL) from MINOS data in the framework of two flavour neutrino oscillations [33, 34]. It should be noted, though, that the derivation of these bounds (the SK one in particular [32]) hinge upon certain assumptions. The primary theoretical assumption relates to the simplification of the system onto a (hybrid) two-flavour scenario. Within the SM paradigm, this approximation is expected to be a very good one. The situation changes considerably, though, once NSI are introduced. As we shall see shortly, the major effect of NSI accrues through matter effects (even in the limit of the ν_e decoupling entirely). However, there exists a nontrivial interplay between such effects and the corresponding matter effects induced by canonical three-flavour oscillations. Consequently, approximations pertaining to the neutrino mixing matrix can significantly alter conclusions reached about NSI. Similarly, the very presence of NSI can leave its imprint in the determination of neutrino parameters. A second set of imponderables relate to statistical and systematic uncertainties, including but not limited to earth density and atmospheric neutrino profiles. Thus, it is quite conceivable that the constraints quoted by the SK collaboration could be relaxed to a fair degree, though perhaps not to the extent of those in Eq. (5). In view of this, and following several other studies [35], we will use a value of $|\varepsilon_{\alpha\beta}| = 0.15$ (for the parameters $\varepsilon_{\mu\tau}$, $\varepsilon_{e\mu}$ and $\varepsilon_{e\tau}$) in our oscillogram diagrams. This value is eminently in agreement with Eq. (5). Note, though, that this choice is essentially to aid visual appreciation of the differences in the oscillogram structures wrought by NSI. Indeed, the experimental sensitivities that we shall be deriving are comparable to (and often significantly better than) those achieved by the SK collaboration. Furthermore, we shall not be taking recourse to two-flavour simplifications to reach such sensitivities. Additionally, the allowed ranges of NSI parameters have been recently extracted using global analysis of neutrino data in Ref. [36].

3 Neutrino oscillation probability in matter with NSI

The purpose of the analytic expressions presented here is to understand the features in the probability in the presence of NSI. All the plots presented in this paper are obtained numerically by solving the full three flavour neutrino propagation equations using the PREM

⁷The SK collaboration uses a different normalization (n_d) while writing the effective NSI parameter (see Eq. (2)) and hence we need to multiply the bounds mentioned in Ref. [32] by a factor of 3.

density profile of the Earth, and the latest values of the neutrino parameters as obtained from global fits (see Table 1).

Oscillation Parameter	Best-fit value	3σ range	Precision (%)
$\sin^2 \theta_{12}/10^{-1}$	3.23	2.78 - 3.75	14.85
$\sin^2 \theta_{23}/10^{-1}$ (NH)	5.67 (4.67) ^a	3.92 - 6.43	24.25
$\sin^2 \theta_{23}/10^{-1}$ (IH)	5.73	4.03 - 6.40	22.72
$\sin^2 \theta_{13}/10^{-2}$ (NH)	2.34	1.77 - 2.94	24.84
$\sin^2 \theta_{13}/10^{-2}$ (IH)	2.40	1.83 - 2.97	23.75
$\delta m_{21}^2 [10^{-5} \text{ eV}^2]$	7.60	7.11 - 8.18	7.00
$ \delta m_{31}^2 [10^{-3} \text{ eV}^2]$ (NH)	2.48	2.30 - 2.65	7.07
$ \delta m_{31}^2 [10^{-3} \text{ eV}^2]$ (IH)	2.38	2.30 - 2.54	5.00
δ/π (NH)	1.34	0.0 - 2.0	-
δ/π (IH)	1.48	0.0 - 2.0	-

^aThis is a local minimum in the first octant of θ_{23} with $\Delta\chi^2 = 0.28$ with respect to the global minimum.

Table 1: Best-fit values and the 3σ ranges for the oscillation parameters used in our analysis [4]. Also given is the precision which is defined as ratio (in percentage) of the difference of extreme values to the sum of extreme values of parameters in the 3σ range. Here NH (IH) refer to normal (inverted) hierarchy.

The analytic computation of probability expressions in presence of SI [37–43] as well as NSI [35, 44–50] has been carried out for different experimental settings by various authors. Note that, for atmospheric neutrinos, one can safely neglect the smaller mass squared difference δm_{21}^2 in comparison to δm_{31}^2 since $\delta m_{21}^2 L/4E \ll 1$ for a large range of values of L and E (especially above a GeV). This “one mass scale dominant” (OMSD) approximation allows for a relatively simple exact analytic formula for the probability (as a function of only three parameters θ_{23} , θ_{13} and δm_{31}^2) for the case of constant density matter [42] with no approximation on s_{13} , and it works quite well⁸. In order to systematically take into account the effect of small parameters, the perturbation theory approach is used. We review the necessary formulation for calculation of probabilities that affect the atmospheric neutrino propagation using the perturbation theory approach [35].

In the ultra-relativistic limit, the neutrino propagation is governed by a Schrödinger-type equation (see [51]) with an effective Hamiltonian

$$\mathcal{H} = \mathcal{H}_{\text{vac}} + \mathcal{H}_{\text{SI}} + \mathcal{H}_{\text{NSI}} , \quad (6)$$

⁸This approximation breaks down if the value of θ_{13} is small since the terms containing δm_{21}^2 can be dropped only if they are small compared to the leading order term which contain θ_{13} . After the precise measurement of the value of θ_{13} by reactor experiments, this approximation is well justified. For multi-GeV neutrinos, this condition ($L/E \ll 10^4 \text{ km/GeV}$) is violated for only a small fraction of events with $E \simeq 1 \text{ GeV}$ and $L \geq 10^4 \text{ km}$.

where \mathcal{H}_{vac} is the vacuum Hamiltonian and $\mathcal{H}_{\text{SI}}, \mathcal{H}_{\text{NSI}}$ are the effective Hamiltonians in presence of SI alone and NSI respectively. Thus,

$$\mathcal{H} = \frac{1}{2E} \left\{ \mathcal{U} \begin{pmatrix} 0 & & \\ & \delta m_{21}^2 & \\ & & \delta m_{31}^2 \end{pmatrix} \mathcal{U}^\dagger + A(x) \begin{pmatrix} 1 + \varepsilon_{ee} & \varepsilon_{e\mu} & \varepsilon_{e\tau} \\ \varepsilon_{e\mu}^* & \varepsilon_{\mu\mu} & \varepsilon_{\mu\tau} \\ \varepsilon_{e\tau}^* & \varepsilon_{\mu\tau}^* & \varepsilon_{\tau\tau} \end{pmatrix} \right\}, \quad (7)$$

where $A(x) = 2E\sqrt{2}G_F n_e(x)$ is the standard CC potential due to the coherent forward scattering of neutrinos and n_e is the electron number density. The three flavour neutrino mixing matrix \mathcal{U} [$\equiv \mathcal{U}_{23} \mathcal{W}_{13} \mathcal{U}_{12}$ with $\mathcal{W}_{13} = \mathcal{U}_\delta \mathcal{U}_{13} \mathcal{U}_\delta^\dagger$ and $\mathcal{U}_\delta = \text{diag}\{1, 1, \exp(i\delta)\}$] is characterized by three angles and a single (Dirac) phase and, in the standard PMNS parameterisation, we have

$$\mathcal{U} = \begin{pmatrix} 1 & 0 & 0 \\ 0 & c_{23} & s_{23} \\ 0 & -s_{23} & c_{23} \end{pmatrix} \begin{pmatrix} c_{13} & 0 & s_{13}e^{-i\delta} \\ 0 & 1 & 0 \\ -s_{13}e^{i\delta} & 0 & c_{13} \end{pmatrix} \begin{pmatrix} c_{12} & s_{12} & 0 \\ -s_{12} & c_{12} & 0 \\ 0 & 0 & 1 \end{pmatrix}, \quad (8)$$

where $s_{ij} = \sin \theta_{ij}$, $c_{ij} = \cos \theta_{ij}$. While, in addition, two Majorana phases are also possible, these are ignored as they play no role in neutrino oscillations. This particular parameterisation along with the fact of \mathcal{H}_{SI} commuting with \mathcal{U}_{23} , allows for a simplification. Going over to the basis, $\tilde{\nu} = \mathcal{U}_{23}^\dagger \nu$, we have $\tilde{\mathcal{H}} = \mathcal{U}_{23}^\dagger \mathcal{H} \mathcal{U}_{23}$ and [47]

$$\begin{aligned} \tilde{\mathcal{H}} = & \lambda \left[\begin{pmatrix} r_A + s_{13}^2 & 0 & c_{13}s_{13}e^{-i\delta} \\ 0 & 0 & 0 \\ c_{13}s_{13}e^{i\delta} & 0 & c_{13}^2 \end{pmatrix} + r_\lambda \begin{pmatrix} s_{12}^2 c_{13}^2 & c_{12}s_{12}c_{13} & -s_{12}^2 c_{13}s_{13}e^{-i\delta} \\ c_{12}s_{12}c_{13} & c_{12}^2 & -c_{12}s_{12}s_{13}e^{-i\delta} \\ s_{12}^2 c_{13}s_{13}e^{i\delta} & -c_{12}s_{12}s_{13}e^{i\delta} & s_{12}^2 s_{13}^2 \end{pmatrix} \right. \\ & \left. + r_A \begin{pmatrix} \tilde{\varepsilon}_{ee} & \tilde{\varepsilon}_{e\mu} & \tilde{\varepsilon}_{e\tau} \\ \tilde{\varepsilon}_{e\mu}^* & \tilde{\varepsilon}_{\mu\mu} & \tilde{\varepsilon}_{\mu\tau} \\ \tilde{\varepsilon}_{e\tau}^* & \tilde{\varepsilon}_{\mu\tau}^* & \tilde{\varepsilon}_{\tau\tau} \end{pmatrix} \right], \quad (9) \end{aligned}$$

where we have defined the ratios

$$\lambda \equiv \frac{\delta m_{31}^2}{2E} \quad ; \quad r_\lambda \equiv \frac{\delta m_{21}^2}{\delta m_{31}^2} \quad ; \quad r_A \equiv \frac{A(x)}{\delta m_{31}^2}. \quad (10)$$

Once again, $\tilde{\mathcal{H}}_{\text{NSI}} = \mathcal{U}_{23}^\dagger \mathcal{H}_{\text{NSI}} \mathcal{U}_{23}$ and the last term in Eq. (9) is

$$\lambda r_A \begin{pmatrix} \varepsilon_{ee} & c_{23}\varepsilon_{e\mu} - s_{23}\varepsilon_{e\tau} & s_{23}\varepsilon_{e\mu} - c_{23}\varepsilon_{e\tau} \\ c_{23}\varepsilon_{e\mu}^* - s_{23}\varepsilon_{e\tau}^* & \varepsilon_{\mu\mu}c_{23}^2 + \varepsilon_{\tau\tau}s_{23}^2 - (\varepsilon_{\mu\tau} + \varepsilon_{\mu\tau}^*)c_{23}s_{23} & \varepsilon_{\mu\tau}c_{23}^2 - \varepsilon_{\mu\tau}^*s_{23}^2 + (\varepsilon_{\mu\mu} - \varepsilon_{\tau\tau})c_{23}s_{23} \\ s_{23}\varepsilon_{e\mu}^* - c_{23}\varepsilon_{e\tau}^* & \varepsilon_{\mu\tau}^*c_{23}^2 - \varepsilon_{\mu\tau}s_{23}^2 + (\varepsilon_{\mu\mu} - \varepsilon_{\tau\tau})c_{23}s_{23} & \varepsilon_{\mu\mu}s_{23}^2 + \varepsilon_{\tau\tau}c_{23}^2 + (\varepsilon_{\mu\tau} + \varepsilon_{\mu\tau}^*)c_{23}s_{23} \end{pmatrix}$$

where $\varepsilon_{\alpha\beta} (\equiv |\varepsilon_{\alpha\beta}| e^{i\phi_{\alpha\beta}})$ are complex. For atmospheric and long baseline neutrinos, $\lambda L \simeq \mathcal{O}(1)$ holds and $r_A L \sim \mathcal{O}(1)$ for a large range of the E and L values considered here. The small quantities are $r_\lambda \simeq 0.03$ and $\tilde{\varepsilon}_{\alpha\beta}$. We decompose $\tilde{\mathcal{H}}$ into two parts : $\tilde{\mathcal{H}} = \tilde{\mathcal{H}}_0 + \tilde{\mathcal{H}}_I$ such that the zeroth order term $\tilde{\mathcal{H}}_0$ provides the effective two flavour limit with $r_A \neq 0$ and $s_{13} \neq 0$ but $r_\lambda = 0$, i.e.,

$$\tilde{\mathcal{H}}_0 = \lambda \begin{pmatrix} r_A(x) + s_{13}^2 & 0 & c_{13}s_{13}e^{-i\delta} \\ 0 & 0 & 0 \\ c_{13}s_{13}e^{i\delta} & 0 & c_{13}^2 \end{pmatrix}, \quad (11)$$

while $\tilde{\mathcal{H}}_I$ contains the other two terms (on the RHS of Eq. (9)) which represent corrections due to non-zero r_λ and the non-zero NSI parameters $\tilde{\varepsilon}_{\alpha\beta}$ respectively. Upon neglecting terms like $r_\lambda s_{13}, r_\lambda s_{13}^2$, we get an approximate form for $\tilde{\mathcal{H}}_I$, viz.,

$$\tilde{\mathcal{H}}_I \approx \lambda \left[r_\lambda \begin{pmatrix} s_{12}^2 & c_{12}s_{12} & 0 \\ c_{12}s_{12} & c_{12}^2 & 0 \\ 0 & 0 & 0 \end{pmatrix} + r_A \begin{pmatrix} \tilde{\varepsilon}_{ee} & \tilde{\varepsilon}_{e\mu} & \tilde{\varepsilon}_{e\tau} \\ \tilde{\varepsilon}_{e\mu}^* & \tilde{\varepsilon}_{\mu\mu} & \tilde{\varepsilon}_{\mu\tau} \\ \tilde{\varepsilon}_{e\tau}^* & \tilde{\varepsilon}_{\mu\tau}^* & \tilde{\varepsilon}_{\tau\tau} \end{pmatrix} \right]. \quad (12)$$

In what follows, we use the perturbation method described in [43] to compute the oscillation probabilities. The exact oscillation probability is given by

$$P_{\alpha\beta} = |S_{\beta\alpha}(x, x_0)|^2, \quad (13)$$

where $S(x, x_0)$ is the evolution matrix defined through $|\nu(x)\rangle = S(x, x_0) |\nu(x_0)\rangle$ with $S(x_0, x_0) = \mathbb{I}$ and satisfying the same Schrödinger equation as $|\nu(x)\rangle$. It can, trivially, be seen to be given by $S(x, x_0) = \mathcal{U}_{23} \tilde{S}(x, x_0) \mathcal{U}_{23}^\dagger$ where $\tilde{S}(x, x_0)$ is independent of θ_{23} . We first evaluate $\tilde{S}(x, x_0)$ using

$$\tilde{S}(x, x_0) = \tilde{S}_0(x, x_0) \tilde{S}_1(x, x_0). \quad (14)$$

Here, $\tilde{S}_0(x, x_0)$ and $\tilde{S}_1(x, x_0)$ satisfy

$$\begin{aligned} i \frac{d}{dx} \tilde{S}_0(x, x_0) &= \tilde{\mathcal{H}}_0(x) \tilde{S}_0(x, x_0); \quad \tilde{S}_0(x_0, x_0) = \mathbb{I}, \\ i \frac{d}{dx} \tilde{S}_1(x, x_0) &= [\tilde{S}_0(x, x_0)^{-1} \tilde{\mathcal{H}}_I(x) \tilde{S}_0(x, x_0)] \tilde{S}_1(x, x_0); \quad \tilde{S}_1(x_0, x_0) = \mathbb{I}. \end{aligned} \quad (15)$$

where $\tilde{\mathcal{H}}_I$ is given by Eq. 12. To the first order in the expansion parameter, we have

$$\tilde{S}(x, x_0) \simeq \tilde{S}_0(x, x_0) - i \tilde{S}_0(x, x_0) \int_{x_0}^x [\tilde{S}_0(x', x_0)^{-1} \tilde{\mathcal{H}}_I(x') \tilde{S}_0(x', x_0)] dx'. \quad (16)$$

Finally, the full evolution matrix $S(x, x_0)$ can be obtained by going back to the original basis from the tilde basis using $S(x, x_0) = \mathcal{U}_{23} \tilde{S}(x, x_0) \mathcal{U}_{23}^\dagger$. The oscillation probability for $\nu_e \rightarrow \nu_\mu$ can be obtained as

$$\begin{aligned} P_{e\mu}^{NSI} &\simeq 4s_{13}^2 s_{23}^2 \left[\frac{\sin^2(1-r_A)\lambda L/2}{(1-r_A)^2} \right] \\ &+ 8s_{13}s_{23}c_{23}(|\varepsilon_{e\mu}|c_{23}c_\chi - |\varepsilon_{e\tau}|s_{23}c_\omega) r_A \left[\frac{\sin r_A \lambda L/2}{r_A} \frac{\sin(1-r_A)\lambda L/2}{(1-r_A)} \cos \frac{\lambda L}{2} \right] \\ &+ 8s_{13}s_{23}c_{23}(|\varepsilon_{e\mu}|c_{23}s_\chi - |\varepsilon_{e\tau}|s_{23}s_\omega) r_A \left[\frac{\sin r_A \lambda L/2}{r_A} \frac{\sin(1-r_A)\lambda L/2}{(1-r_A)} \sin \frac{\lambda L}{2} \right] \\ &+ 8s_{13}s_{23}^2(|\varepsilon_{e\mu}|s_{23}c_\chi + |\varepsilon_{e\tau}|c_{23}c_\omega) r_A \left[\frac{\sin^2(1-r_A)\lambda L/2}{(1-r_A)^2} \right], \end{aligned} \quad (17)$$

where we have used $\tilde{s}_{13} \equiv \sin \tilde{\theta}_{13} = s_{13}/(1-r_A)$ to the leading order in s_{13} , and $\chi = \phi_{e\mu} + \delta$, $\omega = \phi_{e\tau} + \delta$. Only the parameters $\varepsilon_{e\mu}$ and $\varepsilon_{e\tau}$ enter in the leading order expression [45], as

terms such as $r_A \varepsilon_{\alpha\beta}$ have been neglected. Let us discuss the two limiting cases, $r_A \rightarrow 0$ and $r_A \rightarrow 1$. When $r_A \rightarrow 0$, we recover the vacuum limit (given by the first term on the RHS of Eq. (17)). When $r_A \rightarrow 1$, we are close to the resonance condition ($r_A = \cos 2\theta_{13}$ since θ_{13} is small) and the probability remains finite due to the $(1 - r_A)$ and $(1 - r_A)^2$ terms in the denominator of Eq. (17).

The survival probability for $\nu_\mu \rightarrow \nu_\mu$ is given by

$$\begin{aligned}
P_{\mu\mu}^{NSI} \simeq & 1 - s_{2\times 23}^2 \left[\sin^2 \frac{\lambda L}{2} \right] \\
& - |\varepsilon_{\mu\tau}| \cos \phi_{\mu\tau} s_{2\times 23} \left[s_{2\times 23}^2 (r_A \lambda L) \sin \lambda L + 4c_{2\times 23}^2 r_A \sin^2 \frac{\lambda L}{2} \right] \\
& + (|\varepsilon_{\mu\mu}| - |\varepsilon_{\tau\tau}|) s_{2\times 23}^2 c_{2\times 23} \left[\frac{r_A \lambda L}{2} \sin \lambda L - 2r_A \sin^2 \frac{\lambda L}{2} \right], \quad (18)
\end{aligned}$$

where $s_{2\times 23} \equiv \sin 2\theta_{23}$ and $c_{2\times 23} \equiv \cos 2\theta_{23}$. Note that the NSI parameters involving the electron sector do not enter this channel and the survival probability depends only on the three parameters $\varepsilon_{\mu\mu}, \varepsilon_{\mu\tau}, \varepsilon_{\tau\tau}$ [45, 47, 50]. Once again, the vacuum limit is recovered for $r_A \rightarrow 0$. Of these three NSI parameters, $\varepsilon_{\mu\mu}$ is subject to the most stringent constraint (Eq. 5). If we look at $P_{\mu\mu}^{SI}$, the phase factor results in minima of probability for $\lambda L/2 = (2p+1)\pi/2$ (vacuum dip) and maxima for $\lambda L/2 = p\pi$ (vacuum peak) where p is any integer. The oscillation length for the NSI terms, though, is different, and this changes the positions of the peaks and dips.

In order to quantify the impact of NSI, it is useful to define a difference⁹

$$\Delta P_{\alpha\beta} = P_{\alpha\beta}^{SI} - P_{\alpha\beta}^{NSI}, \quad (19)$$

where $P_{\alpha\beta}^{SI}$ is probability of transition assuming standard interactions (*i.e.*, with $\varepsilon_{\alpha\beta}$ being set to zero in Eqs. (17) and (18)) and $P_{\alpha\beta}^{NSI}$ is the transition probability in presence of NSI parameters. For the different channels that are relevant to our study, the quantities $\Delta P_{\alpha\beta}$ are given by

$$\begin{aligned}
\Delta P_{e\mu} \simeq & -8s_{13}s_{23}c_{23}(|\varepsilon_{e\mu}|c_{23}c_\chi - |\varepsilon_{e\tau}|s_{23}c_\omega)r_A \left[\frac{\sin r_A \lambda L/2}{r_A} \frac{\sin(1-r_A)\lambda L/2}{(1-r_A)} \cos \frac{\lambda L}{2} \right] \\
& -8s_{13}s_{23}c_{23}(|\varepsilon_{e\mu}|c_{23}s_\chi - |\varepsilon_{e\tau}|s_{23}s_\omega)r_A \left[\frac{\sin r_A \lambda L/2}{r_A} \frac{\sin(1-r_A)\lambda L/2}{(1-r_A)} \sin \frac{\lambda L}{2} \right] \\
& -8s_{13}s_{23}^2(|\varepsilon_{e\mu}|s_{23}c_\chi + |\varepsilon_{e\tau}|c_{23}c_\omega)r_A \left[\frac{\sin^2(1-r_A)\lambda L/2}{(1-r_A)^2} \right]. \quad (20)
\end{aligned}$$

$$\begin{aligned}
\Delta P_{\mu\mu} \simeq & |\varepsilon_{\mu\tau}| \cos \phi_{\mu\tau} s_{2\times 23} \left(s_{2\times 23}^2 (r_A \lambda L) \sin \lambda L + 4c_{2\times 23}^2 r_A \sin^2 \frac{\lambda L}{2} \right) \\
& - (|\varepsilon_{\mu\mu}| - |\varepsilon_{\tau\tau}|) s_{2\times 23}^2 c_{2\times 23} \left[\frac{r_A \lambda L}{2} \sin \lambda L - 2r_A \sin^2 \frac{\lambda L}{2} \right]. \quad (21)
\end{aligned}$$

⁹The difference used in [35] has an overall sign compared to our definition.

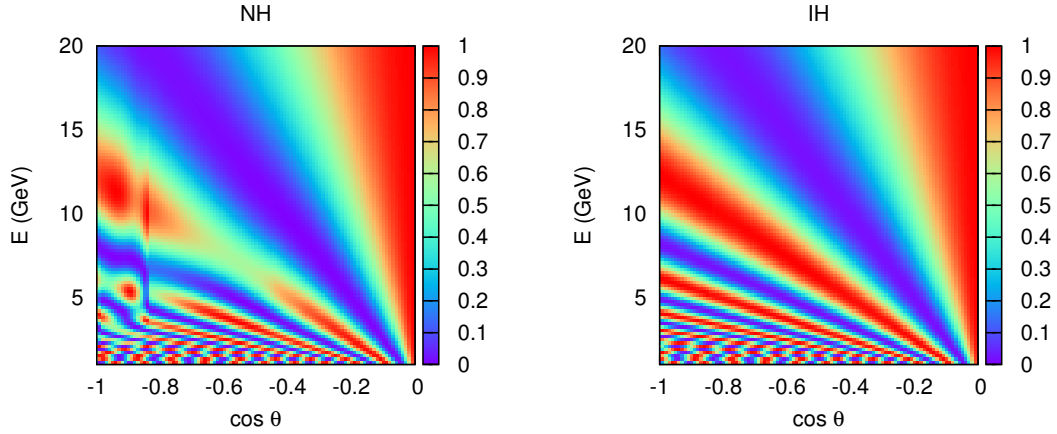


Figure 1: Oscillograms of $P_{\mu\mu}$ for NH and IH with SI alone.

For the case of anti-neutrinos, $A \rightarrow -A$ (which implies that $r_A \rightarrow -r_A$) while $\lambda \rightarrow \lambda, r_\lambda \rightarrow r_\lambda$. Similarly for IH, $\lambda \rightarrow -\lambda, r_\lambda \rightarrow -r_\lambda, r_A \rightarrow -r_A$.

In the present work, for the sake of simplicity, the NSI parameters are taken to be real ($\varepsilon_{\alpha\beta} = \varepsilon_{\alpha\beta}^*$) and also $\delta = 0$.

4 Neutrino oscillograms in presence of NSI :

Within the SM, for a given hierarchy (NH or IH) and best-fit values of the oscillation parameters (as given in Table 1), the oscillation probability depends on only two quantities : the neutrino energy E and the zenith angle of the direction of the neutrino, namely θ , with the vertically downward direction corresponding to $\theta = 0$. The oscillation pattern can, then, be fully described by contours of equal oscillation probabilities in the $E - \cos\theta$ plane. We use these neutrino oscillograms of Earth to discuss the effect of neutrino-matter interactions on the atmospheric neutrinos passing through the Earth (see Refs. [52, 53] for a more detailed discussion of the general features of the SI oscillograms).

$\nu_\mu \rightarrow \nu_\mu$ disappearance channel :

In Fig. 1, we reproduce the neutrino oscillograms in the $\nu_\mu \rightarrow \nu_\mu$ channel for the case of NH (left panel) and IH (right panel) in the $E - \cos(\theta)$ plane. As expected, the muon neutrino

disappearance probability experiences matter effects (MSW effects as well as parametric resonances) for the case of NH but not for the case of IH where it is essentially given by the vacuum oscillation probability (which depends on $\theta_{23}, \Delta m_{32}^2$). For SI in the $\bar{\nu}_\mu \rightarrow \bar{\nu}_\mu$ channel, $A \rightarrow -A$ and the plots for NH and IH get interchanged [42]. In vacuum, the positions of the peaks ($P_{\mu\mu} \simeq 1$) and dips ($P_{\mu\mu} \simeq 0$) can be calculated from the first line on RHS in Eq. (18) as

$$(L/E)^{\text{dip}} \simeq \frac{(2p-1)\pi}{1.27 \times 2 \times \delta m_{31}^2} \text{ km/GeV} \quad ; \quad (L/E)^{\text{peak}} \simeq \frac{k\pi}{1.27 \times \delta m_{31}^2} \text{ km/GeV} \quad (22)$$

where $p, k \in \mathbb{Z}^+$. The first dip and peak, then, are at

$$(L/E)^{\text{dip}} \simeq 499 \text{ km/GeV} \quad ; \quad (L/E)^{\text{peak}} \simeq 998 \text{ km/GeV} \quad (23)$$

which means that for a given L (say $L = 7000$ km or $\cos \theta = -0.549$), we can predict the values of peak energy $E^{\text{peak}} \sim 7$ GeV and dip energy $E^{\text{dip}} \sim 14$ GeV. This can be seen clearly from the right panel of Fig. 1 which corresponds to the IH as the probability in this case is dominated by vacuum oscillations.

L (km)	$\cos \theta$	ρ_{avg} (g/cc)	E^{peak} (GeV)	E^{dip} (GeV)	E_R (GeV)
3000	-0.235	3.33	3.01	6.01	9.00
5000	-0.392	3.68	5.01	10.02	8.14
7000	-0.549	4.19	7.01	14.03	7.15
9000	-0.706	4.56	9.02	18.04	6.57
11000	-0.863	6.15	11.02	22.04	4.87

Table 2: Values of E^{peak} and E^{dip} in vacuum and E_R for $P_{\mu\mu}$ as a function of L , $\cos \theta$ (for the choice of integers p, k mentioned in the text).

The MSW matter effect can occur both in the mantle region as well as the core [54, 55]. The energy at which the MSW resonance takes place in the 13 sector is

$$\rho E_R \simeq \frac{\delta m_{31}^2}{0.76 \times 10^{-4}} \times \cos 2\theta_{13} \text{ GeV g/cc} . \quad (24)$$

Using the values of δm_{31}^2 and θ_{13} from Table 1, we get $E_R \sim 7.15$ GeV for $\rho \simeq 4.19$ g/cc which is the average density for a neutrino traversing ~ 7000 km through the earth¹⁰ to reach the detector. As the neutrino path nears the core, the energy at which the MSW resonance effects occur decreases (see Table 2). As discussed in Ref. [42], when E_R coincides with E^{peak} or E^{dip} , one expects a large change in the probability. We see this feature in the

¹⁰Note, though, that neutrinos of such energies but travelling a smaller path through the earth would also hit regions with $\rho \simeq 4.19$ g/cc and, thus, suffer resonant conversion.

left plot of Fig. 1 around $E_R \sim E^{\text{peak}} \simeq 7$ GeV where the probability is reduced from the peak value by almost 40%. (Note that $L = 7000$ km ($\cos \theta \simeq -0.549$) implies that the neutrino has passed only through the crust and the mantle regions, without penetrating the core.). Also the pattern in the left oscillogram changes abruptly at a value of $\cos \theta_\nu = -0.84$ demarcating two regions : for $\cos \theta < -0.84$, the neutrinos pass through both mantle and core which allows for parametric effects while for $\cos \theta > -0.84$, the neutrinos cross only the mantle region where only the usual MSW effects operate. On the other hand, the parametric resonance occurs when neutrinos traversing the Earth pass through layers of alternating density (mantle-core-mantle) [52, 53].

Having described the case of SI, let us now address the impact of NSI on neutrinos and antineutrinos traversing the Earth. To best illustrate the features, we consider only one NSI parameter to be nonzero. In the leading order expression only two combinations of the three NSI parameters ($\varepsilon_{\mu\tau}, \varepsilon_{\mu\mu}, \varepsilon_{\tau\tau}$) appear. Let us discuss these in turn.

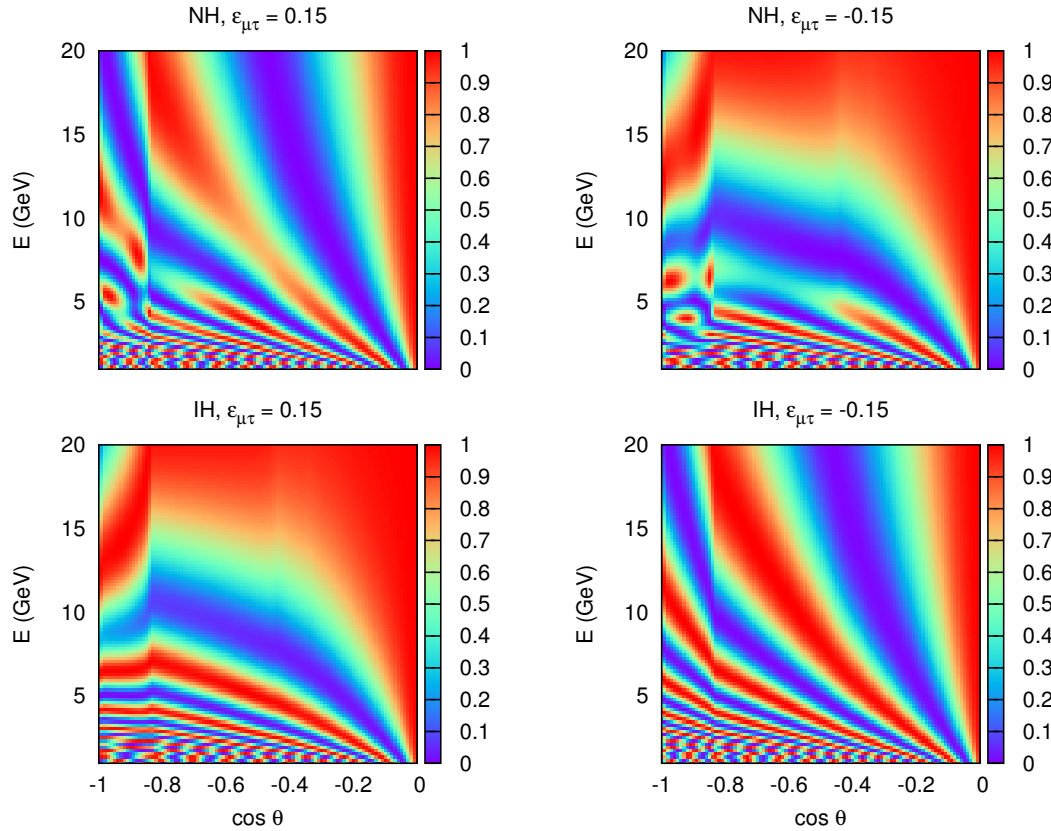


Figure 2: Oscillograms of $P_{\mu\mu}$ for NH and IH with non-zero $\varepsilon_{\mu\tau}$.

(a) $\varepsilon_{\mu\tau} \neq 0; \varepsilon_{\mu\mu} = \varepsilon_{\tau\tau} = 0$: In Fig. 2, we show the corresponding $P_{\mu\mu}^{NSI}$ for the case of NH (top row) and IH (bottom row) and two specific values of the NSI parameter $\varepsilon_{\mu\tau}$ consistent with the current bounds. Note that the case of NH and $\varepsilon_{\mu\tau} > 0$ is grossly similar to the case of IH and $\varepsilon_{\mu\tau} < 0$ (and, similarly, for NH and $\varepsilon_{\mu\tau} < 0$ vs. IH and $\varepsilon_{\mu\tau} > 0$). From Eq. (18), we see that there are two terms proportional to $\varepsilon_{\mu\tau}$, one where the oscillating function is $\sin \lambda L$ with the other being $\sin^2 \lambda L/2$. Thus, the first term can be positive or negative depending upon the value of the phase, while the second term is always positive.

It is the interplay of these two terms that leads to the features in these plots. The mass hierarchy dependence comes from the first term since we have $r_A \lambda L \sin(\lambda L)$ which changes sign when we go from NH to IH. As noted earlier, near the vacuum dip $\lambda L = (2p + 1)\pi/2$, this term will be dominant. Consequently, for NH and $\varepsilon_{\mu\tau} > 0$, the oscillatory pattern is a modification of the standard one. For IH and $\varepsilon_{\mu\tau} > 0$, the term proportional to $|\varepsilon_{\mu\tau}|$ will have a negative overall sign and this leads to washout to a certain extent of the oscillation pattern.

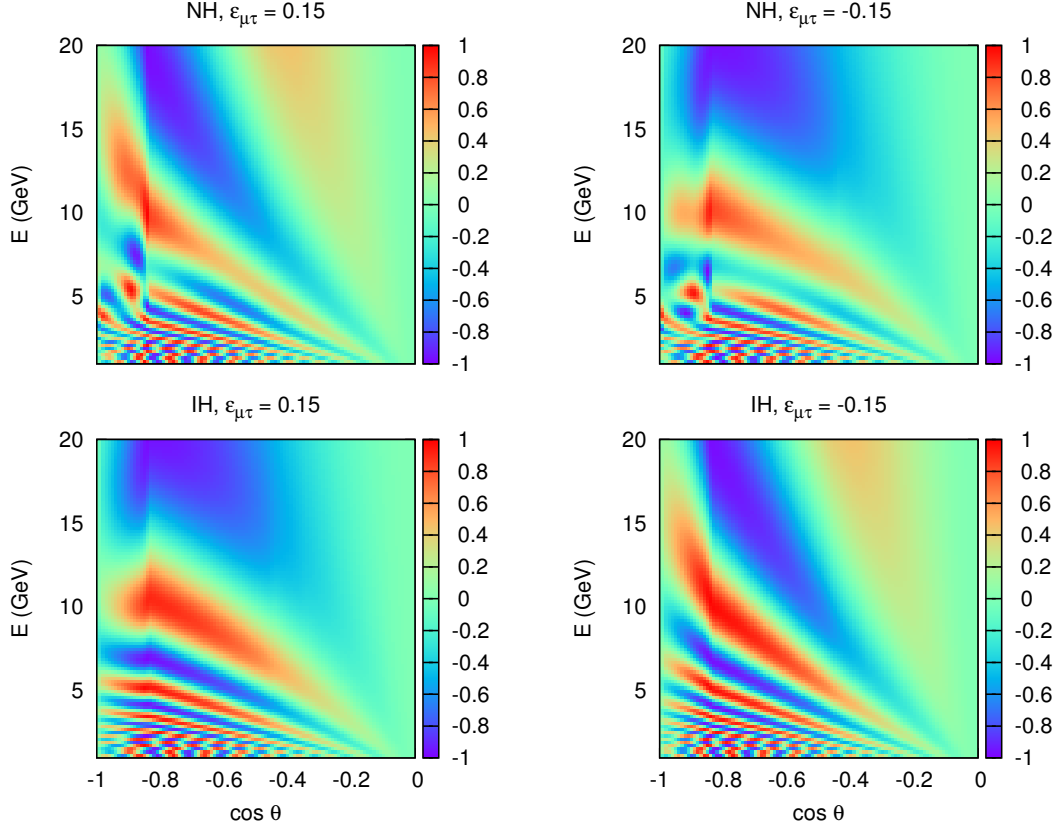


Figure 3: Oscillograms of $\Delta P_{\mu\mu}$ with non-zero $\varepsilon_{\mu\tau}$.

The difference between SI and NSI contributions to the probability $\Delta P_{\mu\mu}$ is shown in Fig. 3. $|\Delta P_{\mu\mu}|$ can be as large as 1 for regions in the core and in mantle for some choice of $\varepsilon_{\mu\tau}$ and hierarchy. We also note large changes in probability (the regions where the difference is large $\sim \pm 1$) along the diagonal line.

(b) $(|\varepsilon_{\mu\mu}| - |\varepsilon_{\tau\tau}|) \neq 0; \varepsilon_{\mu\tau} = 0$: This case will correspond to the case of diagonal FP NSI parameter, $(|\varepsilon_{\mu\mu}| - |\varepsilon_{\tau\tau}|)$. As mentioned above, $|\varepsilon_{\mu\mu}|$ is tightly constrained (see Eq. (5)) while the bound on $|\varepsilon_{\tau\tau}|$ is loose. If we choose $\varepsilon_{\tau\tau} = 0.15$ (and $\varepsilon_{\mu\tau} = 0$), we see that effects due to $\varepsilon_{\tau\tau}$ in $\Delta P_{\mu\mu}$ are insignificant for most baselines except for a tiny region in the core (see Fig. 4). From Eq. 21, only the terms in second line contribute in this case and the minus sign between the two terms lowers the value of $\Delta P_{\mu\mu}$.

(c) Subdominant effects due to $\varepsilon_{e\mu}, \varepsilon_{e\tau} \neq 0$: For the case of NH, we compare the cases of non-zero $\varepsilon_{\mu\tau}, \varepsilon_{e\mu}, \varepsilon_{e\tau}$ in Fig. 4. From Eq. (5), we see that the bounds for $\varepsilon_{e\mu}$ and $\varepsilon_{\mu\tau}$ are

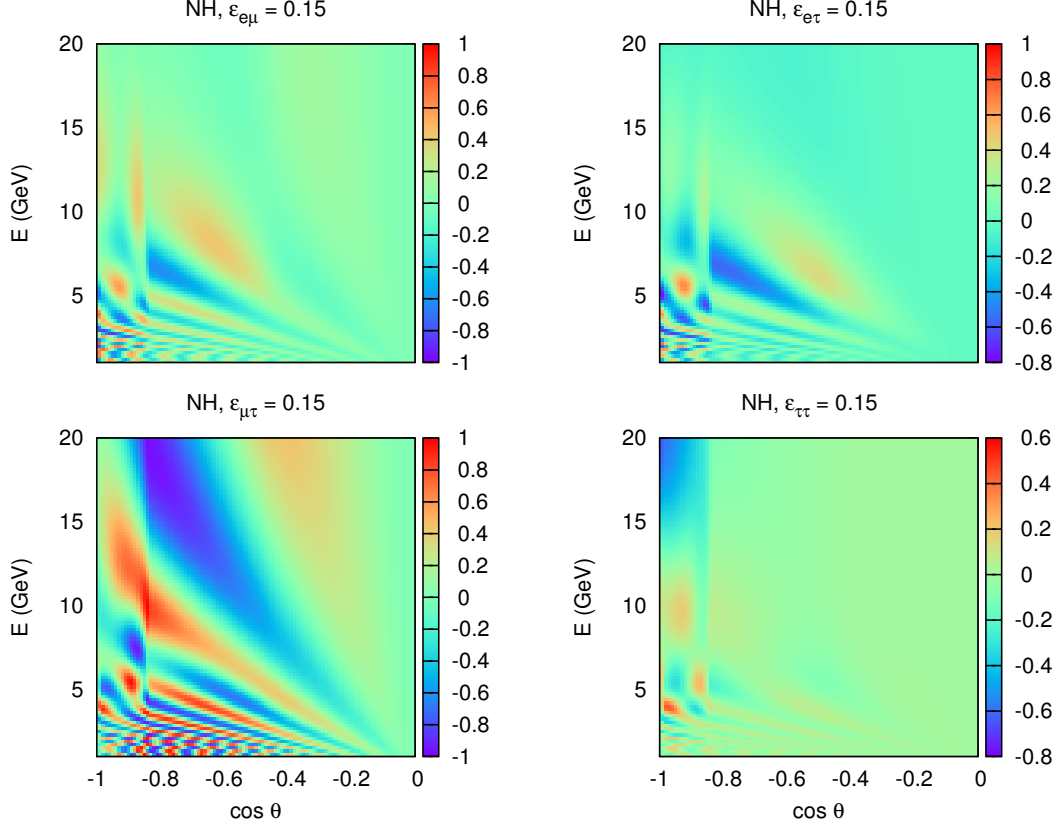


Figure 4: Oscillogram pattern of $\Delta P_{\mu\mu}$ with non-zero $\varepsilon_{e\mu}, \varepsilon_{e\tau}, \varepsilon_{\mu\tau}$ and $\varepsilon_{\tau\tau}$.

similar (0.33) while that on $\varepsilon_{e\tau}$ is rather loose (3.0). It is seen that the other parameters involving the electron sector play only a sub-dominant role in this channel. This can also be understood from the fact that, in the expression for $P_{\mu\mu}^{NSI}$ (see Eq. (18)), these terms appear only at the second order [47].

$\nu_e \rightarrow \nu_\mu$ appearance channel :

In Fig. 5, we have shown the standard neutrino oscillograms in the $\nu_e \rightarrow \nu_\mu$ channel for the case of NH (left panel) and IH (right panel) in the $(E-\cos\theta)$ plane. In this case, the probability is negligible in most parts of the parameter space (especially for the case of IH). The $\nu_e \rightarrow \nu_\mu$ appearance probability in matter differs from that in vacuum in the leading order itself and also the position of peaks and dips of the vacuum curves do not, in general, coincide with those in presence of matter (unlike in the case of muon survival probability). In order to analyse the $P_{e\mu}$ plots, let us look at the OMSD expression [42] (since our analytic expression is valid to first order in θ_{13})

$$P_{e\mu}^{OMSD} = \sin^2 2\tilde{\theta}_{13} \sin^2 \theta_{23} \sin^2 \frac{\delta\tilde{m}_{31}^2 L}{4E} \quad (25)$$

where

$$\sin 2\tilde{\theta}_{13} = \sin 2\theta_{13} \frac{\delta m_{31}^2}{\delta\tilde{m}_{31}^2}$$

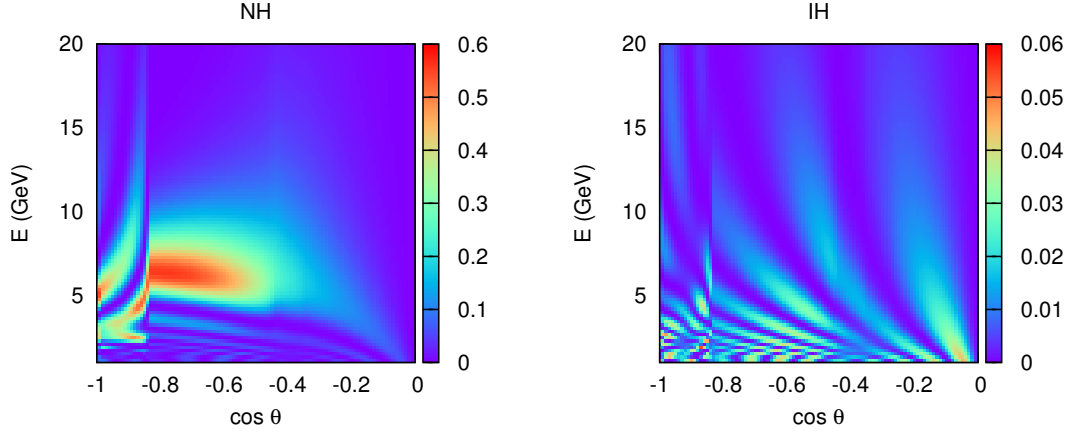


Figure 5: Oscillogram for $P_{e\mu}$ for NH and IH for SI.

$$\delta\tilde{m}_{31}^2 \equiv \sqrt{(\delta m_{31}^2 \cos 2\theta_{13} - A)^2 - (\delta m_{31}^2 \sin 2\theta_{13})^2} \quad (26)$$

The peak energy in matter will be given by [42],

$$(L/E)^{\text{peak}} \simeq \frac{(2p-1)\pi}{1.27 \times 2 \times \delta\tilde{m}_{31}^2} \text{ km/GeV} \quad (27)$$

where $p \in \mathbb{Z}^+$. One would expect $P_{e\mu}$ to be large when the matter peak coincides with the resonance energy, which gives $E_R \simeq 7$ GeV. However, the resonance condition which implies that $\sin 2\tilde{\theta}_{13} = 1$ also leads to $\delta\tilde{m}_{31}^2$ taking its minimum value at resonance energy $\simeq \Delta m_{31}^2 \sin 2\theta_{13}$. Hence, the probability becomes large when $\delta m_{31}^2 \sin 2\theta_{13} L/4E \geq \pi/4$ is satisfied. This gives a value of $L = 10,200$ km for $\sin^2 2\theta_{13} \simeq 0.1$ [42]. Note that the maximum value of $P_{e\mu}$ is given by the value of $\sin^2 \theta_{23} \sim 0.5$. The range of E and $\cos \theta$ where $P_{e\mu}$ is close to its maximal value due to MSW effect is given by $E \in [5, 7.5]$ GeV and $\cos \theta \in [-0.87, -0.5]$ in the mantle region. In the core region, the MSW peak will occur at smaller energies and the parametric resonance leads to large changes.

Having described the case of SI, let us now address the impact of NSI on neutrinos and antineutrinos traversing the Earth. In the leading order expression for $P_{e\mu}^{\text{NSI}}$ (see Eq. (17)) there are only two NSI parameters ($\varepsilon_{e\mu}, \varepsilon_{e\tau}$) that appear whereas $\varepsilon_{\mu\tau}$ does not appear at all. We discuss them in turn.

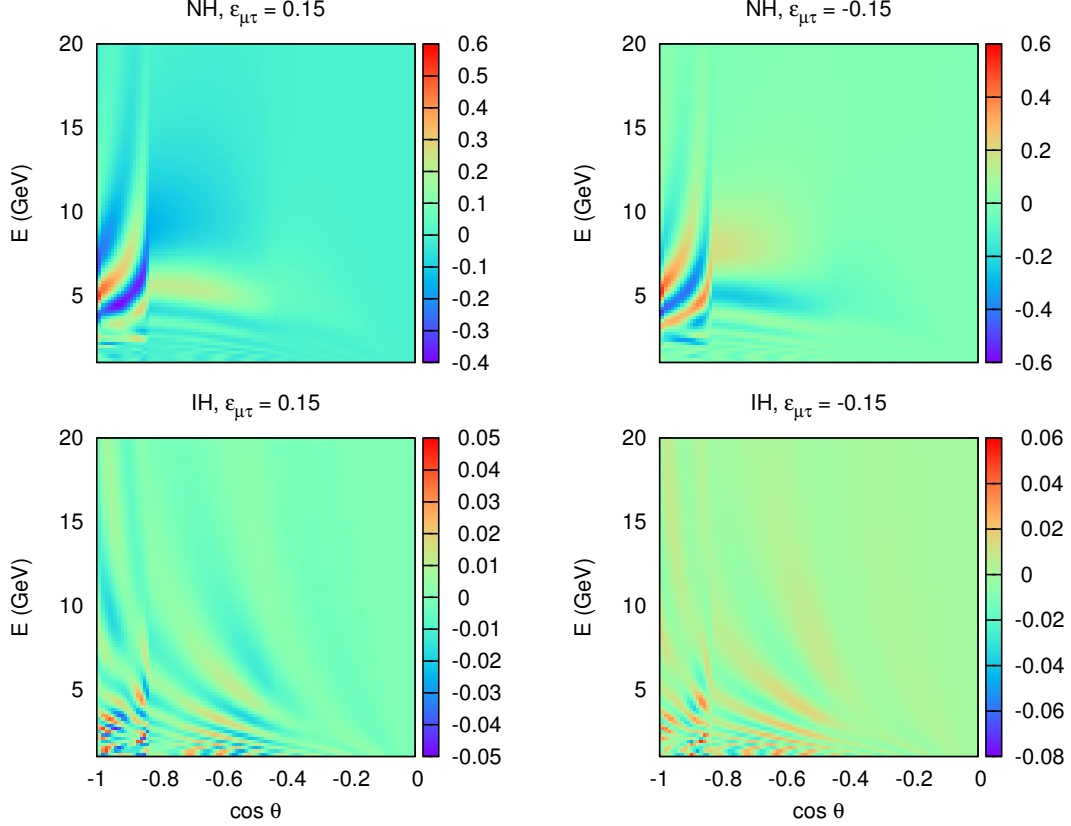


Figure 6: Oscillograms of $\Delta P_{e\mu}$ for NSI parameter $\varepsilon_{\mu\tau}$.

(a) Subdominant effects due to $\varepsilon_{\mu\tau} \neq 0$: In Fig. 6, we show the effect of $\varepsilon_{\mu\tau}$ on the oscillograms of $\Delta P_{e\mu}$. Since the parameter $\varepsilon_{\mu\tau}$ does not appear at all in the first order expression (Eq. (17)), naturally its impact is expected to be small. Consequently, $|\Delta P_{e\mu}| \neq 0$ only in very tiny regions and can at best be as large as $0.3 - 0.4$.

(b) Comparison of effects due to $\varepsilon_{e\mu} \neq 0$, $\varepsilon_{e\tau} \neq 0$, $\varepsilon_{\mu\tau} \neq 0$ and $\varepsilon_{\tau\tau} \neq 0$: In Fig. 7, we compare effects due to four NSI parameters for the case of NH, allowing only one of them to be non-zero at a time. Since the parameters $\varepsilon_{e\mu}, \varepsilon_{e\tau}$ appear in the first order expression (Eq. (17)), they naturally have a larger impact as compared to the other two and, in the favourable situation, $|\Delta P_{e\mu}|$ can be as large as 0.5. This is to be contrasted with $|\Delta P_{\mu\mu}|$ which could take values as large as 1 under favourable conditions. Also, if we look at Eq. (17), we note that $\varepsilon_{e\mu}$ and $\varepsilon_{e\tau}$ appear on equal footing as far as $P_{e\mu}^{NSI}$ is concerned.

5 Simulating an experiment

5.1 Atmospheric events

The neutrino and anti-neutrino CC events are obtained by folding the incident neutrino fluxes with the appropriate probabilities, relevant CC cross sections, the detector efficiency, resolution, mass and the exposure time.

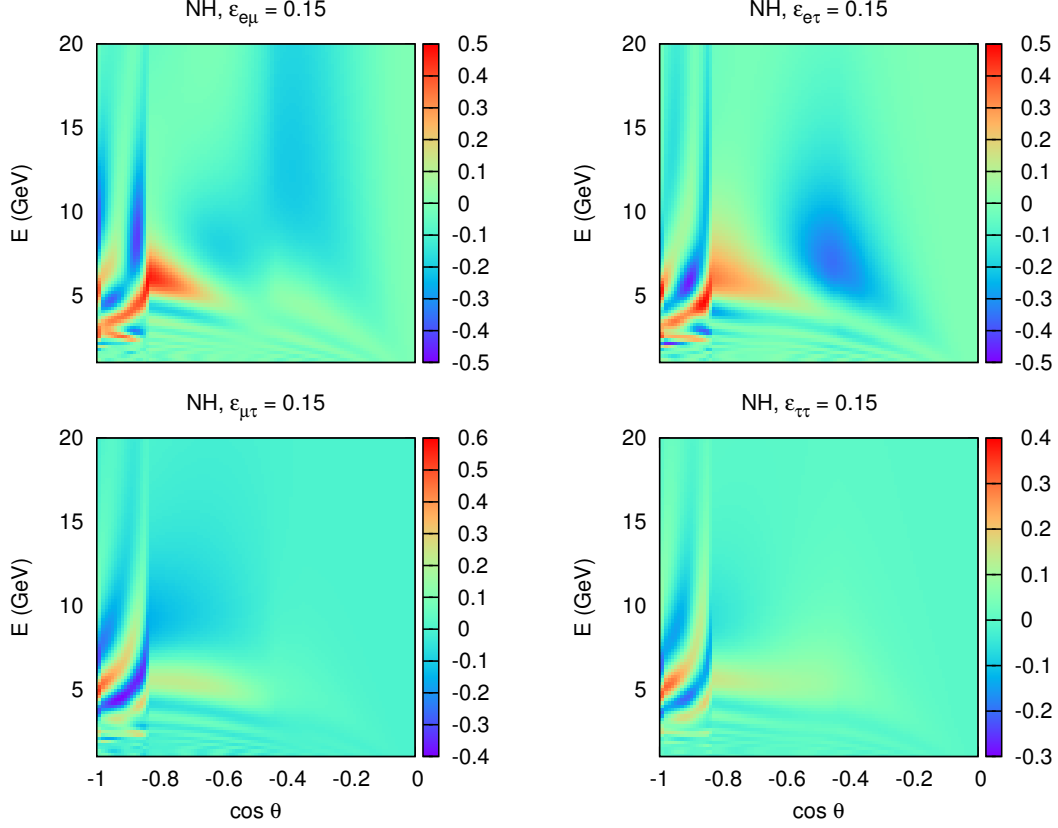


Figure 7: The effect of $\varepsilon_{e\mu}$, $\varepsilon_{e\tau}$, $\varepsilon_{\mu\tau}$ and $\varepsilon_{\tau\tau}$ on the oscillogram of $\Delta P_{e\mu}$.

The μ^- event rate in a specific energy bin of width dE and the angle bin of width $d\Omega$ can be written as

$$\frac{d^2 N_\mu}{d\Omega dE} = \frac{1}{2\pi} \left[\left(\frac{d^2 \Phi_\mu}{d \cos \theta dE} \right) P_{\mu\mu} + \left(\frac{d^2 \Phi_e}{d \cos \theta dE} \right) P_{e\mu} \right] \sigma_{CC}(\nu_\mu) D_{\text{eff}}(\mu^-). \quad (28)$$

Here $\Phi_{\mu,e}$ are the atmospheric fluxes (ν_μ and ν_e), σ_{CC} is the total CC cross section and D_{eff} is the detector efficiency. We have used the Honda atmospheric neutrino flux and cross-sections as given in [56]. Similarly, the μ^+ event rate can be obtained using the anti-neutrino flux, probability and cross section, and the efficiency for μ^+ (nominally, the same as for μ^-). Analogously, the e^- event rates would be given by

$$\frac{d^2 N_e}{d\Omega dE} = \frac{1}{2\pi} \left[\left(\frac{d^2 \Phi_\mu}{d \cos \theta dE} \right) P_{\mu e} + \left(\frac{d^2 \Phi_e}{d \cos \theta dE} \right) P_{ee} \right] \sigma_{CC}(\nu_e) D_{\text{eff}}(e^-), \quad (29)$$

with the e^+ event rate being expressed in terms of anti-neutrino fluxes, probabilities and cross sections as well $D_{\text{eff}}(e^+)$.

In a realistic detector, the energy and angular resolution is not infinite, and to mimic this, we consider a Gaussian resolution function, R . For the energy resolution function, we use

$$R_{\text{EN}}(E_t, E_m) = \frac{1}{\sqrt{2\pi}\sigma} \exp \left[-\frac{(E_m - E_t)^2}{2\sigma^2} \right], \quad (30)$$

where E_m and E_t denote the measured and true values of energy respectively. The smearing width σ is a function of E_t itself. The functional form of σ for ICAL and LAr detectors are given in Table. 4 and 5. Similarly, the angular smearing function is given by

$$R_\theta(\Omega_t, \Omega_m) = N \exp \left[- \frac{(\theta_t - \theta_m)^2 + \sin^2 \theta_t (\phi_t - \phi_m)^2}{2 (\Delta\theta)^2} \right], \quad (31)$$

where N is a normalisation constant.

The experimentally observable ν_μ event rates would, thus, be given by

$$\frac{d^2 N_\mu}{d\Omega_m dE_m} = \frac{1}{2\pi} \int \int dE_t d\Omega_t R_{EN}(E_t, E_m) R_\theta(\Omega_t, \Omega_m) [\Phi_\mu^d P_{\mu\mu} + \Phi_e^d P_{e\mu}] \sigma_{CC} D_{\text{eff}}, \quad (32)$$

and similarly for the ν_e . Here we have denoted $(d^2\Phi/d\cos\theta dE)_{\mu,e} \equiv \Phi_{\mu,e}^d$ *etc.*. We limit the charged lepton phase space to $E_\ell \in [1, 10]$ GeV and $\cos\theta \in [-1.0, -0.1]$ which covers the incident atmospheric neutrinos propagating through the earth. For effecting a statistical analysis, we subdivide the energy ($\cos\theta$) range into 9 (18) equal bins each.

It is worth noting at this stage that even if we incorporate the full detector simulation for detectors such as the Iron Calorimeter (ICAL) at INO or a generic Liquid Argon (LAr) one (such as in Ref. [57]), the essential physics points of the present work would not change. Since these studies are not yet available for full-fledged reconstruction of neutrino energy and angle using muons and hadrons, we adopt a simpler approach as mentioned above.

5.2 χ^2 analysis

We quantify the difference between the events with SI and NSI in terms of a χ^2 function. For a fixed set of parameters, the latter is calculated using the method of pulls, which allows us to take into account the various statistical and systematic uncertainties (such as those on the fluxes, cross sections *etc.*).

Let $N_{ij}^{\text{th}}(\text{std})$ be the theoretical event rate for the i - j^{th} bin, as calculated with the standard values for the inputs. Now, let us allow the k^{th} input (known with an uncertainty σ_k) to deviate from its standard value by an amount $\sigma_k \xi_k$. If the relative uncertainties are not very large, the change in N_{ij}^{th} can be expressed as a linear function of the *pull* variables ξ_k . In other words, the value of N_{ij}^{th} with the changed inputs is given by

$$N_{ij}^{\text{th}} = N_{ij}^{\text{th}}(\text{std}) + \sum_{k=1}^{\text{npull}} c_{ij}^k \xi_k, \quad (33)$$

where npull is the number of sources of uncertainty, which in our case is 5. The systematic uncertainties are given in Table. 3. With these changed inputs, the goodness of fit is quantified in terms of a modified χ^2 function defined as

$$\chi^2(\xi_k) = \sum_{i,j} \frac{\left[N_{ij}^{\text{th}}(\text{std}) + \sum_{k=1}^{\text{npull}} c_{ij}^k \xi_k - N_{ij}^{\text{ex}} \right]^2}{N_{ij}^{\text{ex}}} + \sum_{k=1}^{\text{npull}} \xi_k^2 \quad (34)$$

Uncertainty	Value (in %)
Flux Normalization	20
Tilt Factor	5
Zenith angle dependence	5
Cross section	10
Detector systematics	5

Table 3: Different uncertainties used in our χ^2 analysis.

where the additional term ξ_k^2 is the penalty imposed for moving the k^{th} input away from its standard value by $\sigma_k \xi_k$. The χ^2 with pulls, which includes the effects of all theoretical and systematic uncertainties, is obtained by minimizing $\chi^2(\xi_k)$, given in Eq. (34), with respect to all the pulls ξ_k , viz.

$$\chi_{\text{pull}}^2 = \text{Min}_{\xi_k} [\chi^2(\xi_k)] . \quad (35)$$

Note that ICAL magnetised detector will be able to distinguish muon neutrinos and muon anti-neutrinos and hence the effective χ^2 is given by $\chi_{\mu^-}^2 + \chi_{\mu^+}^2$. On the other hand, the χ^2 for the (unmagnetised) LIAR detector is $\chi^2 = \chi_{\mu^- + \mu^+}^2 + \chi_{e^- + e^+}^2$. Finally, we marginalize the χ^2 over the allowed range of the oscillation parameters as mentioned in Table 1.

6 Event spectrum for the two detector types

We describe the details used for the two detector types (ICAL and LAr) used in our analysis :

ICAL detector

This is a large magnetised iron detector and is being planned for the INO experiment in South India. It consists of 151 layers of magnetized iron plates interleaved with Resistive Plate Chambers (RPC) as active detector elements with a total mass of about 52 kilotons. Such a detector is capable of detecting muons (especially for GeV energies) and identify their charge by virtue of the magnetization. Additionally, the ICAL can detect hadronic showers. The energy and angular resolution of muons and hadrons for the ICAL have been obtained from the INO simulation code and using that information the initial neutrino energy and angle can be reconstructed. The detailed specifications are given in Table 4.

Energy Resolution ($\sigma(E)$)	$0.1\sqrt{E}$
Angular Resolution ($\Delta\theta$)	10°
Detector efficiency (\mathcal{E})	85%

Table 4: ICAL Detector parameters in the atmospheric neutrino experiment simulation [58].

In Fig. 8, the ν_μ events are shown. At low energies, the number of events is around ~ 100 for all the zenith angles both for the case of SI and NSI ($\varepsilon_{\mu\tau} \neq 0$). The difference with and

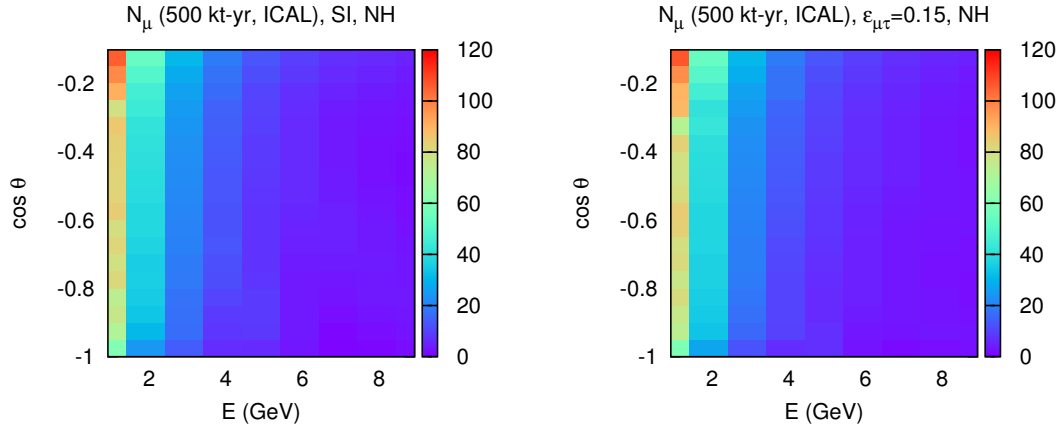


Figure 8: ν_μ events with SI and with NSI for non-zero $\varepsilon_{\mu\tau}$ (left). All the data are generated for 500 kT-yr of exposure for magnetized ICAL assuming NH as the true hierarchy.

without NSI of the ν_μ events using parameters $\varepsilon_{\mu\tau}$ and $\varepsilon_{\mu e}$ is shown in Fig. 9. For ICAL, it is evident that $\Delta N_\mu \simeq \pm 10$ in some of the bins for $\varepsilon_{\mu\tau} \neq 0$ while for $\varepsilon_{\mu e} \neq 0$, $\Delta N_\mu \sim \pm 4$. This was expected since the leading dependence was through $\varepsilon_{\mu\tau}$, corroborates the probability level analysis.

LAr detector

A LAr detector is capable of detecting not only muons but also electrons, and has a very good angular resolution. Since the detector is unmagnetised, only the total events of a given flavour can be measured. For the proposed Long Baseline Neutrino Experiment (which is designated to operate with a beam and a baseline of 1300 km), a 35 kt unmagnetized LAr detector is to be placed underground to study atmospheric neutrinos along with the beam. The specifications for the LAr detector are given in Table 5. We shall assume here a 10-yr operation period, or, equivalently, an effective fiducial volume of 350 kt-yr.

The difference of the total muon ($\nu_\mu + \bar{\nu}_\mu$) and electron ($\nu_e + \bar{\nu}_e$) neutrino events with and without NSI are shown in Fig. 10. LAr detector is complementary to ICAL as the impact of $\varepsilon_{\mu\tau}$ is less compared to $\varepsilon_{\mu e}$ for both muon and electron flavours.

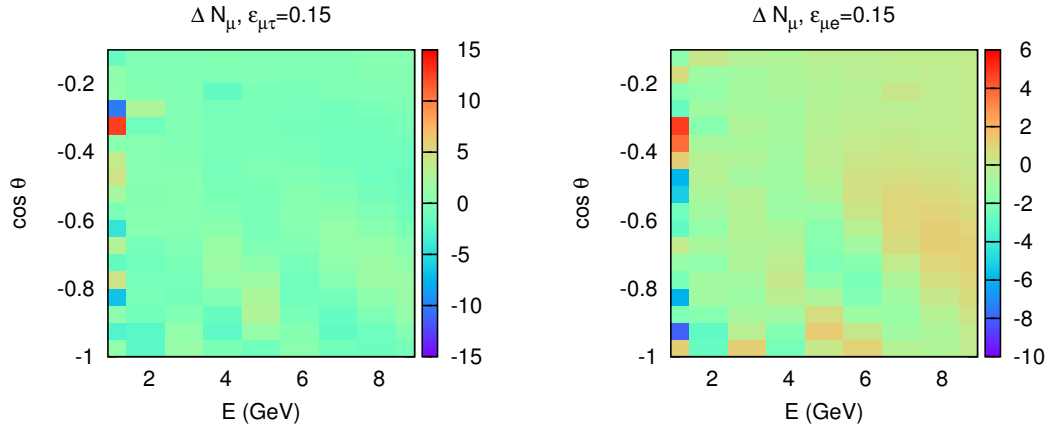


Figure 9: The difference with and without NSI of ν_μ (only) events for non-zero $\varepsilon_{\mu\tau}$ (left) and $\varepsilon_{\mu e}$ (right). All the data are generated for 500 kT-yr of exposure for magnetized ICAL assuming NH as the true hierarchy.

Rapidity (y)	0.45 for ν 0.30 for $\bar{\nu}$
Energy Resolution ($\sigma(E)$)	$\sqrt{(0.01)^2 + (0.15)^2/(yE) + (0.03)^2}$
Angular Resolution ($\Delta\theta$)	3.2° for ν_μ 2.8° for ν_e
Detector efficiency (\mathcal{E})	85%

Table 5: The LAr detector parameters used for the atmospheric neutrino experiment simulation [59, 60].

7 Results and Conclusions

We have considered the effect of NSI in the analysis of atmospheric neutrino oscillation experiments. To this end, we consider two detector types, *viz.* a magnetised iron one (the specifications being those for the proposed ICAL) and a generic unmagnetized LAr detector and contrast the capabilities of these two detector types for individual NSI parameters. With the constraints on $\varepsilon_{\mu\mu}$ already being very stringent [31], we assume it is nonexistent, and concentrate on the others that such detectors can be sensitive to, namely $\varepsilon_{\mu\tau}$, $\varepsilon_{\mu e}$ and

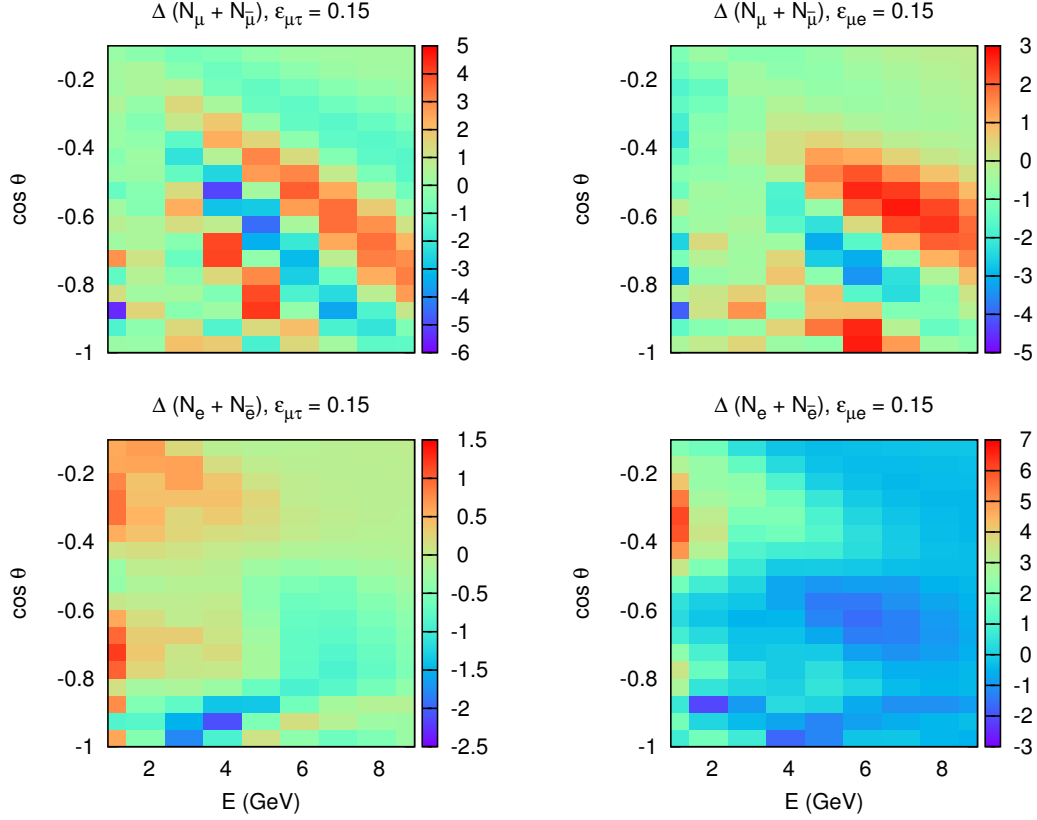


Figure 10: The difference with and without NSI of the total muon neutrino events ($\nu_\mu + \bar{\nu}_\mu$) and total electron neutrino events ($\nu_e + \bar{\nu}_e$). All the data are generated for 350 kT-yr of exposure for unmagnetized LAr detector assuming NH as the true hierarchy.

$\varepsilon_{e\tau}$.

In Fig 11, we show the variation of $\Delta\chi^2$ (for the individual detector choices) with the aforementioned parameters. For the sake of simplicity, in each case, we vary only one of these parameters, assuming the other two to be vanishing identically. For each plot, the horizontal dotted maroon line represents the 3σ CL bound that is expected to be reached.

As far as $\varepsilon_{\mu\tau}$ is concerned, the dominant contribution comes from muon events and the ICAL detector would perform better than a LAr detector both for the case of NH and IH (see Figs. 11(a) and 11(b)). This is primarily due to the fact that the ICAL detector is magnetized which allows it to distinguish between μ^+ and μ^- events. In contrast, the unmagnetized LAr detector can detect electron as well as muon events but is not able to identify charge of the leptons. The charge identification capability of ICAL allows us to add the two individual $\Delta\chi^2$ corresponding to the μ^- and μ^+ events respectively. For ICAL, the net $\Delta\chi^2$ is a sum of $\Delta\chi_{\mu^-}^2$ and $\Delta\chi_{\mu^+}^2$. For the LAr detector, the net $\Delta\chi^2$ comes from $\Delta\chi_{e^-+e^+}^2$ and $\Delta\chi_{\mu^-+\mu^+}^2$ and the lack of charge identification capability leads to poorer sensitivity.

As far as $\varepsilon_{e\tau}$ is concerned, the probabilities involving only the electron sector would play a role and the LAr detector is expected to perform better than the ICAL detector (see

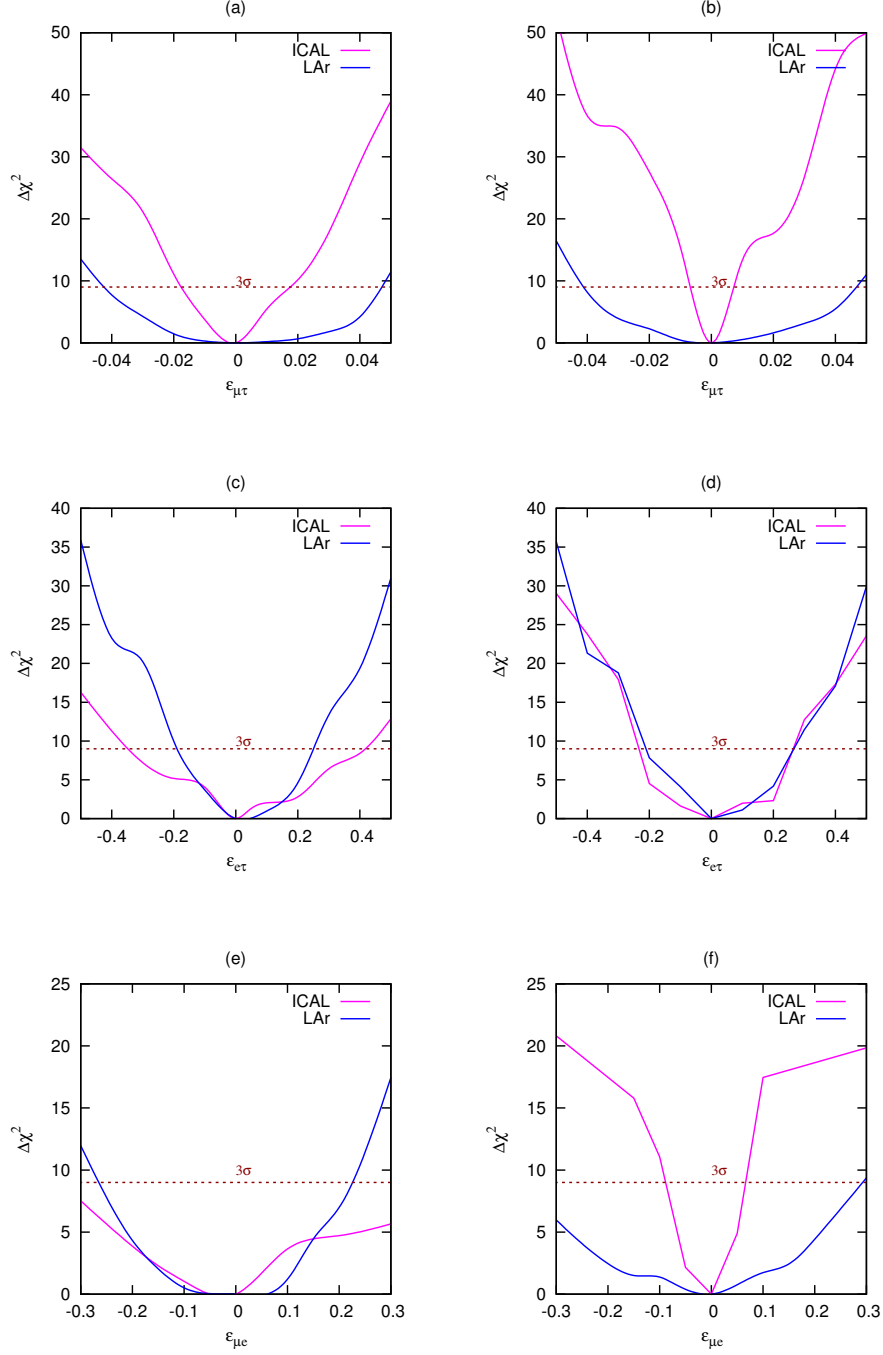


Figure 11: $\Delta\chi^2$ vs $\varepsilon_{\mu\tau}$, $\varepsilon_{e\tau}$ and $\varepsilon_{\mu e}$ for NH (left) and IH (right) for the two detector types.

Figs. 11(c) and 11(d)). For NH, comparing the two plots (Figs. 11(a) and 11(c)), we see analogous effect for the case of NH with a role reversal of the two detectors. But for IH, comparing the Figs. 11(b) and 11(d), we note that for $e - \tau$ sector, there is very little

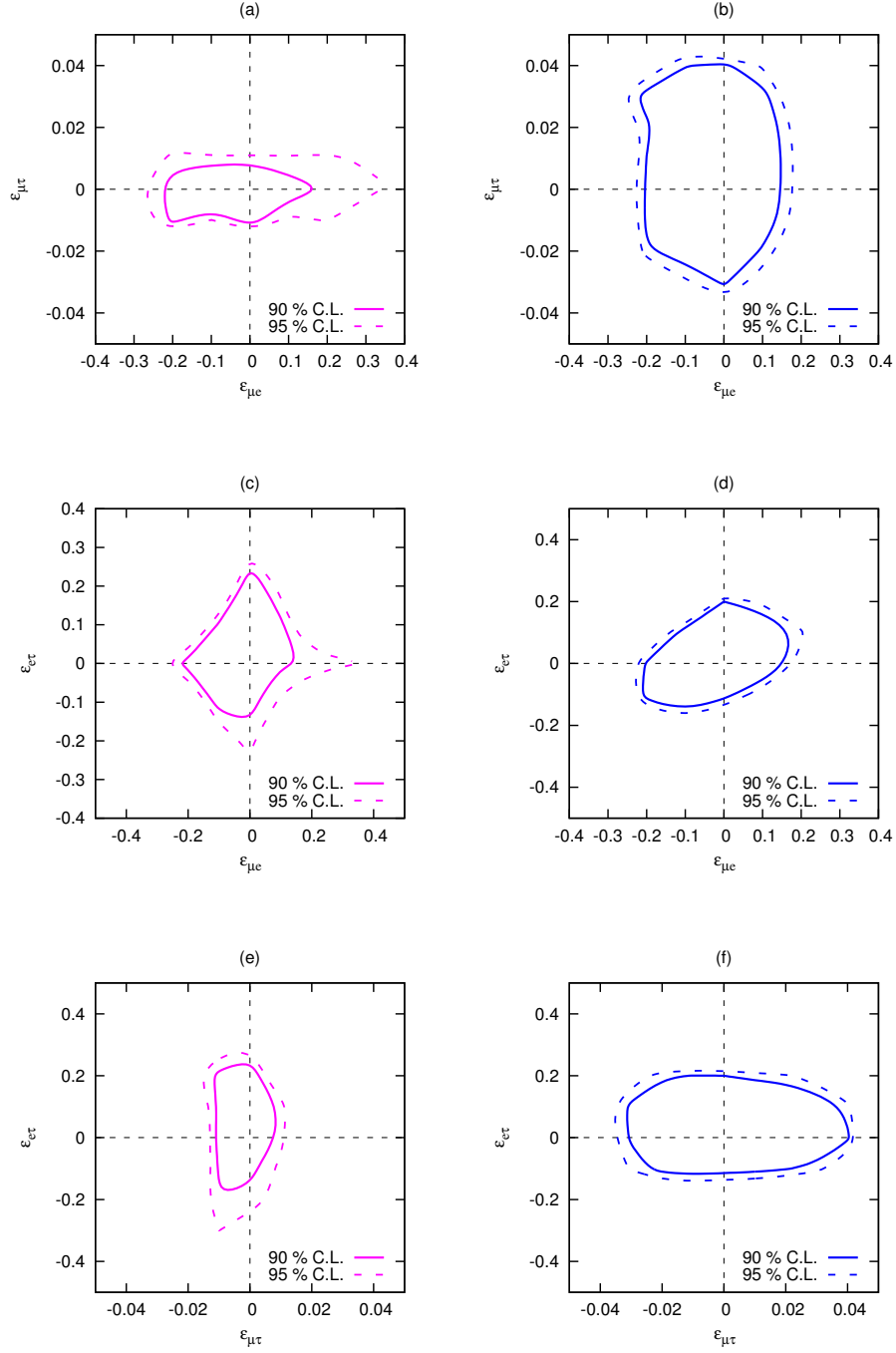


Figure 12: Constraints on pairs of NSI parameters for different detector types. Left panel is for 500 kt-yr of fiducial volume of ICAL and right panel with 350 kt-yr unmagnetized LAr detector. NH is assumed to be true hierarchy.

difference between the curves of the two detectors and this is due to the fact that it is not possible to isolate the e^- and e^+ events (as the LAr detector is not magnetized). Another

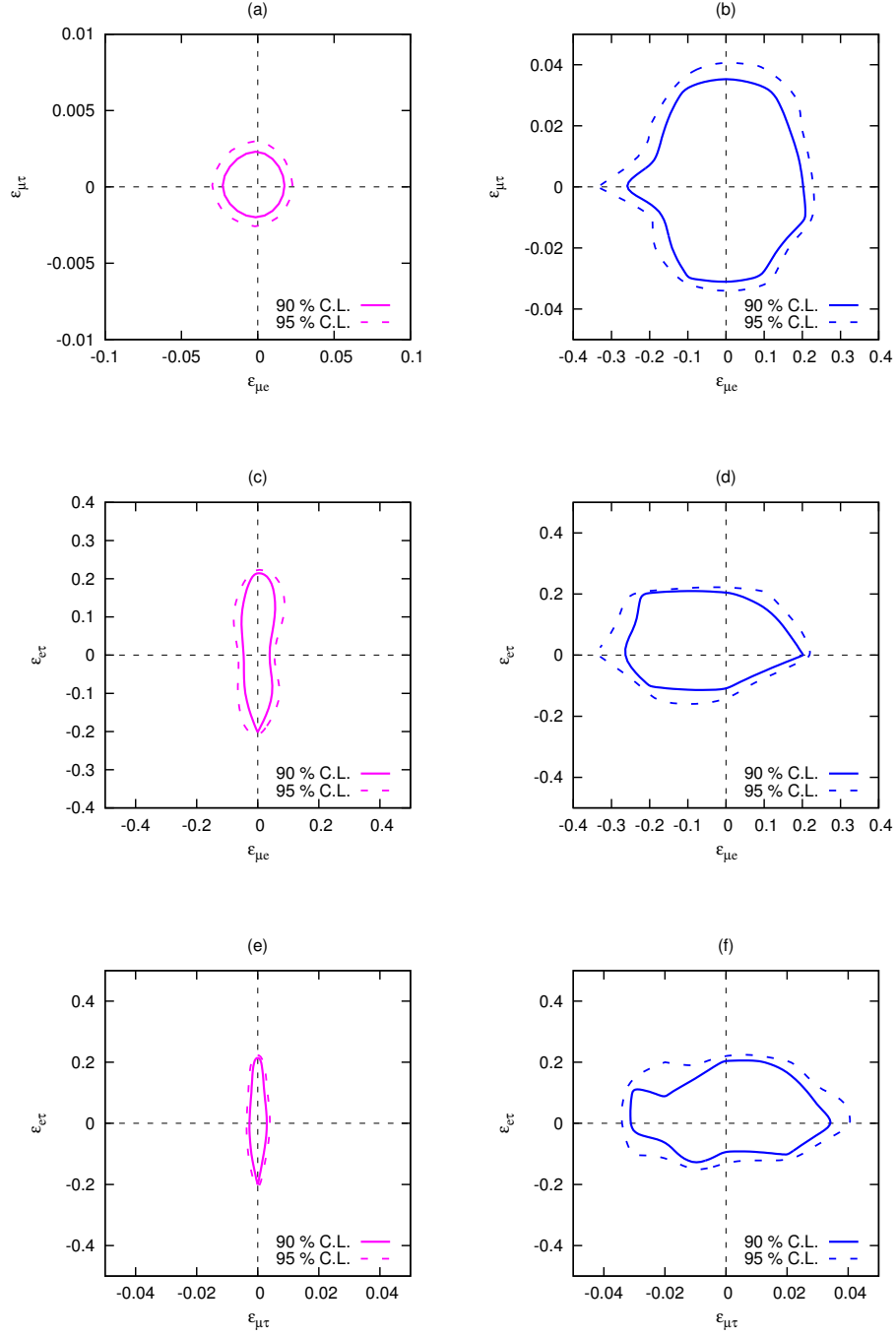


Figure 13: Constraints on pairs of NSI parameters for different detector types. Left panel is for 500 kt-yr of fiducial volume of ICAL and right panel with 350 kt-yr unmagnetized LAr detector. IH is assumed to be true hierarchy.

intriguing aspect is that the $\Delta\chi^2$ plot is asymmetric in the case of IH for the parameter $\varepsilon_{e\tau}$.

A nonzero $\varepsilon_{\mu e}$ manifests its presence in each of $P_{\mu\mu}$, $P_{\mu e}$, $P_{e\mu}$ and P_{ee} with the first two being more relevant, given the initial fluxes. Naively, thus, one would expect the LAr detector to do better than the ICAL one. Once again, though, the charge resolution can be crucial. For the NH case, the LAr does win, but only marginally, and that too for large $|\varepsilon_{\mu e}|$ (where the ability to detect electron events becomes important). On the other hand, for the IH case, the structure of the matter effects ensures that the ICAL does much better.

It is worthwhile to look at the results above through the prism of mass hierarchy. For the inverted scenario, the ICAL, thus, does significantly better than a LAr detector for each of $\varepsilon_{\mu\tau}$ and $\varepsilon_{\mu e}$, while for $\varepsilon_{e\tau}$ the two perform similarly. The reason is not difficult to fathom. With $P_{\mu\mu}$ playing a major role in each of the first two cases, the charge distinguishability available at the ICAL rules the day, while this advantage is lost in the third. More intriguingly, the significantly better performance of the LAr for negative $\varepsilon_{e\tau}$ can be traced back to the facilitation of the matter effect.

On the other hand, for NH, ICAL (LAr) does better for $\varepsilon_{\mu\tau}$ ($\varepsilon_{e\tau}$) whereas the performance is largely similar for $\varepsilon_{\mu e}$. Note that, for $\varepsilon_{\mu\tau}$, the superiority of the ICAL is now less pronounced than it is for the inverted case. This degradation of the ICAL sensitivity, as well the corresponding one for $\varepsilon_{e\tau}$ can be traced back to the oscillograms of Sec. 4. As the plots of $\Delta P_{\mu\mu}$ and $\Delta P_{\mu e}$ (Fig. 3 and 6) show, there are larger regions in $E - \cos\theta$ parameter space in case of IH than NH for $\Delta P_{\mu\mu}$. Quite the opposite is seen for $\Delta P_{\mu e}$ - the regions with large change in probability actually shrink for IH compared to NH. But, since the contribution from $P_{\mu e}$ to N_μ is suppressed by the electron to muon flux ratio for the atmospheric neutrinos and also the maximum possible change is $\sim \pm 0.5$ (which is much smaller than $\sim \pm 1$ for $\Delta P_{\mu\mu}$), this does not nullify the large changes induced due to $P_{\mu\mu}$. It is, thus, amply clear that the unravelling of NSI parameters requires detectors with complementary properties.

Expectedly, different experimental systematics can lead to a quantitative change on the NSI parameters. However we believe that the choices we have made in this work are realistic, and we expect that other choices will not qualitatively alter the conclusions presented.

These observations are also reflected in Fig. 12 and 13 where the constraints on pairs of NSI parameters, $\varepsilon_{\mu\tau} - \varepsilon_{\mu e}$, $\varepsilon_{e\tau} - \varepsilon_{\mu e}$ and $\varepsilon_{e\tau} - \varepsilon_{\mu\tau}$ are shown for the case of NH and IH. The allowed values of pairs of NSI parameters imply that we can demarcate between SI and NSI for those values at a given confidence level. For ICAL (LAr) detector, the solid magenta (blue) line corresponds to 90% C.L. while the dashed magenta (blue) line corresponds to 95% C.L. The results are also summarised in Table 6 for the two detector types for NH and IH. For ICAL, the expected sensitivity is better in case of IH in comparison to NH for the parameters $\varepsilon_{\mu\tau}$ and $\varepsilon_{\mu e}$ unlike the case in [61] where the sensitivities in the two cases are comparable. This is due to the fact that we have not used priors on standard parameters. We assume that the other experiments will significantly reduce the error bars on the standard parameters by the time these future atmospheric neutrino experiments are operational. For the $\varepsilon_{\mu\tau}$, we note that the bounds for ICAL are comparable to the ones obtained in [61] while for $\varepsilon_{\mu e}$ and $\varepsilon_{e\tau}$ our bounds are roughly a factor of two higher than those obtained in [61].

ICAL (NH)	ICAL (IH)	LAr (NH)	LAr (IH)
$-0.02 < \varepsilon_{\mu\tau} < 0.01$	$-0.005 < \varepsilon_{\mu\tau} < 0.005$	$-0.03 < \varepsilon_{\mu\tau} < 0.04$	$-0.03 < \varepsilon_{\mu\tau} < 0.035$
$-0.21 < \varepsilon_{\mu e} < 0.15$	$-0.07 < \varepsilon_{\mu e} < 0.05$	$-0.2 < \varepsilon_{\mu e} < 0.15$	$-0.25 < \varepsilon_{\mu e} < 0.20$
$-0.2 < \varepsilon_{e\tau} < 0.23$	$-0.2 < \varepsilon_{e\tau} < 0.2$	$-0.12 < \varepsilon_{e\tau} < 0.2$	$-0.15 < \varepsilon_{e\tau} < 0.2$

Table 6: Comparison of sensitivities offered by the two detectors for NH and IH at 90% CL. We assume 500 kt-yr in case of ICAL and 350 kt-yr in case of LAr detector (see Fig. 12 and 13).

Acknowledgments :

We would like to thank Brajesh Choudhary and Silvia Pascoli for discussions during the initial stages of this work and Tommy Ohlsson for helpful email correspondence. We acknowledge the use of HRI cluster facility to carry out computations in this work. We thank Mehedi Masud for crucial help with the plots. AC thanks the INO Collaboration, Atri Bhattacharya, Sandhya Choubey, Amol Dighe and Pomita Ghoshal for useful discussions. DC and PM acknowledge the European Union grant FP7 ITN INVISIBLES (Marie Curie Actions, PITN-GA-2011-289442). DC also acknowledges the grant SR/MF/PS-02/2013-DUB from the Dept. of Science and Technology, India. RG acknowledges support from Fermi National Accelerator Laboratory in the form of an Intensity Frontier fellowship. PM acknowledges support from German Academic Exchange Service (DAAD) for her visit to DESY, Zeuthen during which a major part of this work was carried out and support from University Grants Commission under the second phase of University with Potential of Excellence at JNU.

References

- [1] Y. Fukuda *et al.* (Super-Kamiokande Collaboration), Phys.Rev.Lett. **81**, 1562 (1998), hep-ex/9807003.
- [2] M. Gonzalez-Garcia, M. Maltoni, J. Salvado, and T. Schwetz, JHEP **1212**, 123 (2012), 1209.3023.
- [3] F. Capozzi, G. Fogli, E. Lisi, A. Marrone, D. Montanino, *et al.*, Phys.Rev. **D89**, 093018 (2014), 1312.2878.
- [4] D. V. Forero, M. Tórtola, and J. W. F. Valle, Phys. Rev. D **90**, 093006 (2014), URL <http://link.aps.org/doi/10.1103/PhysRevD.90.093006>.
- [5] T. Ohlsson, Rept.Prog.Phys. **76**, 044201 (2013), 1209.2710.
- [6] Y. Grossman, Phys.Lett. **B359**, 141 (1995), hep-ph/9507344.

- [7] M. C. Gonzalez-Garcia, M. M. Guzzo, P. I. Krastev, H. Nunokawa, O. L. G. Peres, V. Pleitez, J. W. F. Valle, and R. Zukanovich Funchal, Phys. Rev. Lett. **82**, 3202 (1999).
- [8] A. Pilaftsis and T. E. Underwood, Phys.Rev. **D72**, 113001 (2005), [hep-ph/0506107](#).
- [9] R. Barbieri and R. N. Mohapatra, Phys.Lett. **B218**, 225 (1989).
- [10] K. Babu and R. Mohapatra, Phys.Rev.Lett. **63**, 228 (1989).
- [11] D. Choudhury and U. Sarkar, Phys.Lett. **B235**, 113 (1990).
- [12] K. J. Healey, A. A. Petrov, and D. Zhuridov, Phys.Rev. **D87**(11), 117301 (2013), [1305.0584](#).
- [13] J. R. Bhatt, B. R. Desai, E. Ma, G. Rajasekaran, and U. Sarkar, Phys.Lett. **B687**, 75 (2010), [0911.5012](#).
- [14] C. Wetterich, Nuclear Physics B **897**, 111 (2015), ISSN 0550-3213, URL <http://www.sciencedirect.com/science/article/pii/S0550321315001790>.
- [15] N. Fornengo, M. Maltoni, R. Tomas, and J. Valle, Phys.Rev. **D65**, 013010 (2002), [hep-ph/0108043](#).
- [16] P. Huber and J. Valle, Phys.Lett. **B523**, 151 (2001), [hep-ph/0108193](#).
- [17] M. Gonzalez-Garcia and M. Maltoni, Phys.Rev. **D70**, 033010 (2004), [hep-ph/0404085](#).
- [18] M. Gonzalez-Garcia, M. Maltoni, and J. Salvado, JHEP **1105**, 075 (2011), [1103.4365](#).
- [19] A. Esmaili and A. Y. Smirnov, JHEP **1306**, 026 (2013), [1304.1042](#).
- [20] A. Datta, R. Gandhi, P. Mehta, and S. U. Sankar, Physics Letters B **597**(34), 356 (2004).
- [21] A. Chatterjee, R. Gandhi, and J. Singh, JHEP **1406**, 045 (2014), [1402.6265](#).
- [22] A. Esmaili, D. Gratieri, M. Guzzo, P. de Holanda, O. Peres, *et al.*, Phys.Rev. **D89**, 113003 (2014), [1404.3608](#).
- [23] A. Esmaili, O. Peres, and Z. Tabrizi, Journal of Cosmology and Astroparticle Physics **2014**(12), 002 (2014), URL <http://stacks.iop.org/1475-7516/2014/i=12/a=002>.
- [24] A. Esmaili, F. Halzen, and O. Peres, JCAP **1211**, 041 (2012), [1206.6903](#).
- [25] A. Esmaili, F. Halzen, and O. Peres, JCAP **1307**, 048 (2013), [1303.3294](#).
- [26] A. Esmaili and A. Y. Smirnov, JHEP **1312**, 014 (2013), [1307.6824](#).
- [27] A. Datta, R. Gandhi, B. Mukhopadhyaya, and P. Mehta, Phys.Rev. **D64**, 015011 (2001), [hep-ph/0011375](#).
- [28] P. Mehta, S. Dutta, and A. Goyal, Phys.Lett. **B535**, 219 (2002), [hep-ph/0107214](#).

- [29] C. Biggio, M. Blennow, and E. Fernandez-Martinez, JHEP **0908**, 090 (2009), 0907.0097.
- [30] S. Davidson, C. Pena-Garay, N. Rius, and A. Santamaria, JHEP **0303**, 011 (2003), hep-ph/0302093.
- [31] F. Escribuela, M. Tortola, J. Valle, and O. Miranda, Phys.Rev. **D83**, 093002 (2011), 1103.1366.
- [32] G. Mitsuka *et al.* (Super-Kamiokande Collaboration), Phys.Rev. **D84**, 113008 (2011), 1109.1889.
- [33] P. Adamson *et al.* (MINOS Collaboration), Phys.Rev. **D88**(7), 072011 (2013), 1303.5314.
- [34] J. Kopp, P. A. Machado, and S. J. Parke, Phys.Rev. **D82**, 113002 (2010), 1009.0014.
- [35] T. Ohlsson, H. Zhang, and S. Zhou, Phys.Rev. **D88**(1), 013001 (2013), 1303.6130.
- [36] M. Gonzalez-Garcia and M. Maltoni, JHEP **1309**, 152 (2013), 1307.3092.
- [37] V. D. Barger, K. Whisnant, S. Pakvasa, and R. Phillips, Phys.Rev. **D22**, 2718 (1980).
- [38] A. Cervera, A. Donini, M. Gavela, J. Gomez Cadenas, P. Hernandez, *et al.*, Nucl.Phys. **B579**, 17 (2000), hep-ph/0002108.
- [39] R. Gandhi, P. Ghoshal, S. Goswami, P. Mehta, and S. U. Sankar, Phys.Rev.Lett. **94**, 051801 (2005), hep-ph/0408361.
- [40] D. Indumathi and M. Murthy, Phys.Rev. **D71**, 013001 (2005), hep-ph/0407336.
- [41] D. Choudhury and A. Datta, JHEP **0507**, 058 (2005), hep-ph/0410266.
- [42] R. Gandhi, P. Ghoshal, S. Goswami, P. Mehta, and S. U. Sankar, Phys.Rev. **D73**, 053001 (2006), hep-ph/0411252.
- [43] E. K. Akhmedov, R. Johansson, M. Lindner, T. Ohlsson, and T. Schwetz, JHEP **0404**, 078 (2004), hep-ph/0402175.
- [44] N. Ribeiro, H. Minakata, H. Nunokawa, S. Uchinami, and R. Zukanovich-Funchal, JHEP **0712**, 002 (2007), 0709.1980.
- [45] J. Kopp, M. Lindner, T. Ota, and J. Sato, Phys.Rev. **D77**, 013007 (2008), 0708.0152.
- [46] M. Blennow and T. Ohlsson, Phys. Rev. **D78**, 093002 (2008), 0805.2301.
- [47] T. Kikuchi, H. Minakata, and S. Uchinami, JHEP **0903**, 114 (2009), 0809.3312.
- [48] D. Meloni, T. Ohlsson, and H. Zhang, JHEP **04**, 033 (2009), 0901.1784.
- [49] K. Asano and H. Minakata, JHEP **1106**, 022 (2011), 1103.4387.

- [50] P. Coloma, A. Donini, J. Lopez-Pavon, and H. Minakata, JHEP **1108**, 036 (2011), 1105.5936.
- [51] G. G. Raffelt, *Stars as Laboratories for Fundamental Physics: The Astrophysics of Neutrinos, Axions, and Other Weakly Interacting Particles* (University of Chicago Press, 1996).
- [52] E. K. Akhmedov, M. Maltoni, and A. Y. Smirnov, JHEP **0705**, 077 (2007), hep-ph/0612285.
- [53] E. K. Akhmedov, M. Maltoni, and A. Y. Smirnov, JHEP **0806**, 072 (2008), 0804.1466.
- [54] L. Wolfenstein, Phys. Rev. **D17**, 2369 (1978).
- [55] S. P. Mikheev and A. Y. Smirnov, Sov. Phys. Usp. **30**, 759 (1987).
- [56] T. K. Gaisser and M. Honda, Ann. Rev. Nucl. Part. Sci. **52**, 153 (2002), hep-ph/0203272.
- [57] A. Chatterjee, K. Meghna, K. Rawat, T. Thakore, V. Bhatnagar, *et al.*, JINST **9**, P07001 (2014), 1405.7243.
- [58] A. Chatterjee, P. Ghoshal, S. Goswami, and S. K. Raut, JHEP **1306**, 010 (2013), 1302.1370.
- [59] A. Bueno, Z. Dai, Y. Ge, M. Laffranchi, A. Melgarejo, *et al.*, JHEP **0704**, 041 (2007), hep-ph/0701101.
- [60] V. Barger, R. Gandhi, P. Ghoshal, S. Goswami, D. Marfatia, *et al.*, Phys.Rev.Lett. **109**, 091801 (2012), 1203.6012.
- [61] S. Choubey, A. Ghosh, T. Ohlsson, and D. Tiwari, JHEP **12**, 126 (2015), 1507.02211.